MRI OF DEGENERATIVE JOINT DISEASE IN THE MUSCULOSKELETAL SYSTEM

By

Habib Al saleh

A dissertation submitted in partial fulfillment

of the requirements for the degree of

Doctor of Philosophy

(Medical Physics)

at the

UNIVERSITY OF WISCONSIN – MADSION

2013

Date of final oral examination: 11/27/2013

The dissertation is approved by the following members of the Final Oral Committee:

Walter F. Block, Professor, Professor, Medical Physics
Richard Kijowski, Professor, Associate Professor (CHS), Radiology
Charles A. Mistretta, Professor, Professor, Medical Physics
Andrew L. Alexander, Professor, Professor, Medical Physics
Oliver Wieben, Professor, Associate Professor, Medical Physics
Kevin M. Johnson, Scientist, Assistant Scientist, Medical Physics

Abstract

While MRI adequately serves the needs of assessing acute injuries to the musculoskeletal system today, MRI's full potential as tool in assessing the degree and causes of chronic, degenerative processes in the musculoskeletal system are unmet. Three-dimensional radial sequences are superior to two-dimensional sequences for high resolution MR imaging. These techniques may play an important role in the diagnostic of osteoarthritis patients specifically in evaluating the articular cartilage. Here we adapted an existing high performing imaging method for acquiring high isotropic resolution fat-suppressed knee joint images. The performance of this sequence for evaluating the articular cartilage of the knee joint at 3.0T was compared with conventional MRI three dimensional sequences. Higher SNR and CNR were achieved for cartilage and synovial fluid in comparison to the conventional counterpart. Some connective tissues in joints give low signal and are invisible with standard MR protocols. In the second part of this work, we developed a novel imaging method to robustly decompose signal into channels of ultrashort water relaxation, longer water relaxation, and fat by incorporating changes to the IDEAL chemical species separation algorithm. The method was effective in phantom and in vivo studies and has the potential to be utilized for segmenting a variety of tissue types. Finally, the effects of 3D under sampling under conditions of high isotropic resolution and fixed scan time were quantified in vivo imaging and benefits of increased coil elements investigated. Preliminary results comparing an 8-channel and 16-channel coil are included. 16-channel images showed dramatically improved detail and better joint depiction with increased acceleration factor compared to standard 8-channel knee coil.

Acknowledgements

I would like to express my gratitude to all those who gave me the possibility to complete this thesis. First and foremost I wish to thank my advisor, Professor Wally Block who offered his continuous advice and encouragement throughout the course of this thesis. His guidance helped me in all the time of research and writing of this thesis. I could not have imagined having a better advisor for my Ph.D study. Thank you Wally!

In addition, I would like to thank my committee, Dr. Richard Kijowski, Dr. Charles Mistretta, Dr. Oliver Wieben, Dr. Andrew Alexander and Dr. Kevin Johnson for their support, guidance and helpful suggestions. Their guidance has served me well and I owe them my heartfelt appreciation.

I wish to thank my entire extended family who encouraged me and prayed for me throughout the time of my research. My brothers, my sisters, my uncles, and my cousins were particularly supportive.

Lastly, I would like to thank my family for all their love and encouragement. I especially thank my parents for showing faith in my. And most of all for my loving, supportive, encouraging, and patient wife Afaf whose faithful support during the final stages of this Ph.D. is so appreciated. Thank you

I dedicate this thesis to

my paranets, my wife, Afaf, and my beloved kids, Ali and Hussain

for their constant support and unconditional love.

Table of contents

Table of Contents

Outline

Chapter 1 *Background:*

A brief description of 3D radial imaging and a description of bSSFP sequence with Alternating repletion time imaging for fat suppression is first provided. Next, a review of two dimensional and three dimensional Ultrashort TE (UTE) imaging followed by a summary of fat/water separation using Dixon technique specially with iterative decomposition of water and fat with echo asymmetry and least-squares estimation (IDEAL) is presented.

Chapter 2 Alternating Repetition Time Balanced SSP Imaging for Cartilage Assessment:

This chapter contains a comparison study of Vastly Undersampled Isotropic Projection Imaging (VIPR) with Fat-Suppressed Alternating Repetition Time balanced Steady-State Free-Precession (FS-ATR SSFP) sequence with other currently used fat-suppressed three-dimensional sequences for evaluating the articular cartilage of the knee joint at 3.0T. Both quantitative and more subjective measures of image quality are presented.

Chapter 3 High Contrast 3D IDEAL Ultrashort TE (UTE) Imaging:

This chapter presents a new signal model for chemical shift-based water-fat separation method with the 3D ultra short echo time (UTE) data acquisition for imaging and quantification of the short T_2 tissues with robust fat and long T2 suppression. The validation of this new method is demonstrated with simulation of a digital phantom created with fat, water and short T_2 components. High resolution images of both knee joint and Achilles tendon are shown.

Chapter 4 Improved Performance with 16 Channel Coil: Quantification of Unedersampling Artifacts with 8 and 16 Channel Knee Coils:

Chapter 4 demonstrate a quantitative and qualitative study of the aliasing noise in radial under sampled knee joint imaging using MR coil arrays with 16 channel counts and compare results with the GE 8 channel coil.

Chapter 5 Imaging of Joint Structure with Limited Free Water Using UTE imaging method:

In this chapter, I demonstrates an improved selective excitation of short T2 components in 3T joint imaging using Inverted Double Half RF (IDHRF) pulse UTE imaging with improved long T_2 suppression and reduced eddy current. It provides applications of IDHRF in the knee and challis tendon joints imaging.

Chapter 1:

Background

Osteoarthritis (OA) is one of the most prevalent chronic diseases in the United States(1)(2)(3)(4)(5)(6). Magnetic resonance (MR) imaging has recently been identified by the Outcome Measures in Rheumatologic Clinical Trials (OMERACT) and the Osteoarthritis Research Society International (OARSI) as the most appropriate imaging modality to assess joint degeneration in OA research studies(7). However, the mechanism of the pain in OA is believed to involve multiple pathways including all joint structures(8)(9)(10)(11)(12)(13)(14). For these reasons, OMERACT and OARSI have recommended that MR protocols in OA research studies should provide "whole-organ" joint assessment(7)(15).

While current physiologic cartilage imaging techniques are highly sensitive for detecting early cartilage degeneration, their long scan times, ranging between 10 and 20 minutes for a single plane acquisition, significantly limits their use in OA research studies(16–23)(24–26)(27). Whole-organ" MR protocols used in OA research studies should be designed primarily to assess articular cartilage, but should also evaluate other joint structures which may cause pain and mechanical dysfunction in patients with OA. These protocols should provide detailed cartilage analysis using high resolution morphologic methods to identify focal and diffuse cartilage loss and to obtain accurate and precise cartilage volume measurements. "Whole-organ" MR

protocols should also include imaging methods which can evaluate ligaments, tendons, menisci, bone, and synovium which can also be sources of pain in patients with OA.

General Imaging Mechanisms Utilized: From Spin Echo to Steady-state

Many of the method utilized in this paper move from spin-echo imaging to steady-state imaging, both bSSFP for T2-like imaging and spoiled gradient –recalled echo imaging for UTE imaging. Next a more in-depth description of current steady-state method and the use of radial encoding in these methods to produce high resolution imaging is provided.

1.1 3D Radial Imaging

Non-Cartesian data sampling, such as radial and spiral encoding, is often used for fast data acquisition in MRI to capture the rapidly decaying signals. Therefore, these trajectories are increasingly used in various applications such as cardiac imaging, MR angiography and musculoskeletal imaging. In contrast to Cartesian sampling, which requires a gradient for phase encoding before data acquisition and a refocusing gradient after data acquisition, the 3d radial trajectory starts at the center of k-space and move outward with no need to rephase or refocus the magnetization before or after data acquisition, allowing more time to collect data. Compared to Cartesian trajectories, 3D radial sampling offers several advantages such as improved robustness against motion artifacts and short TE and TR times with reduced sensitivity to susceptibility effects.

The 3D-Radial technique known as Vastly undersampled Isotropic Projection Reconstruction (VIPR) (28)(29), is used to limit the scan time in 3D radial sampling by acquiring significantly

fewer projections than would be required to meet the Nyquist criteria. Undersampling in radial imaging does not affect resolution because spatial resolution in radial imaging is determined by the readout resolution. The double-half-echo PR technique is used with VIPR to significantly increases the acquisition efficiency. Furthermore, with the acquisition of dual-half-echoes, useful phase information may be used to suppress unwanted fat signal. Figure 1.1 shows the dual half-echo VIPR pulse sequence and its k-space trajectory. In this sequence, data acquisition starts at the k-space origin and moves outward to the edge of k-space, collecting one radial line, and then a gradient blip is applied to makes a small rotation, allowing a second radial line to be collected while returning to the origin(30).

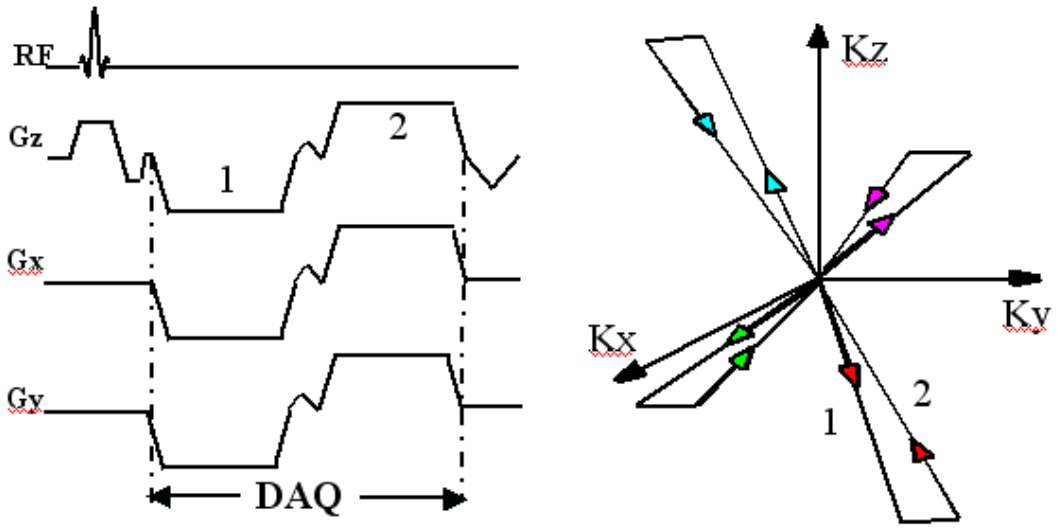

Figure 1.1 Double half echo VIPR sequence diagram and its corresponding k-space trajectory. Data acquisition starts at origin of k-space outward to edge of k-space collecting half radial line, making small blip and return back to origin collecting second half radial line of k-space.

1.2 BSSFP Imaging with Alternating Repetition Time

Steady-state free precession (SSFP) imaging is an MRI technique which uses steady states of longitudinal and transverse magnetizations. Transverse coherences from overlapping multi-order spin echoes and stimulated echoes are usually accomplished by refocusing the phase-encoding gradient in each repetition time (TR). Fully balanced Steady-state free precession (bSSFP) imaging is a special case of SSFP imaging where all imaging gradients are refocused within each TR (31). Balanced SSFP imaging achieves high signal-to-noise ratios (SNR) efficiency within short repetition times. Contrast in bSSFP is given by the ratio of T1 and T2. However, because fat has high T2/T1 ratio, bSSFP techniques yield undesirably high fat signal intensity that obscure nearby tissues. So, bSSFP sequences are usually combined with a fat suppression method to improve conspicuity of the desired water signal (32)(33).

In the conventional bSSFP sequence a series of RF pulses are applied rapidly and repeatedly with the same interpulse intervals (TR) and same flip angle while alternating the phases of the RF pulses by 180°. The SSFP spectral response is comprised of broad passbands separated by narrow notches spaced 1/TR apart. One way of suppressing fat in bSSFP is to selectively choose a TR such that fat fall within the spectral notch in SSFP. However, this technique is ineffective because width of this stopband is too narrow to give a robust selection of fat. Linear combination SSFP (LCSSFP) separates fat and water by exploiting the relative difference in phase each species experiences in two passes with different RF phase cycling (34).

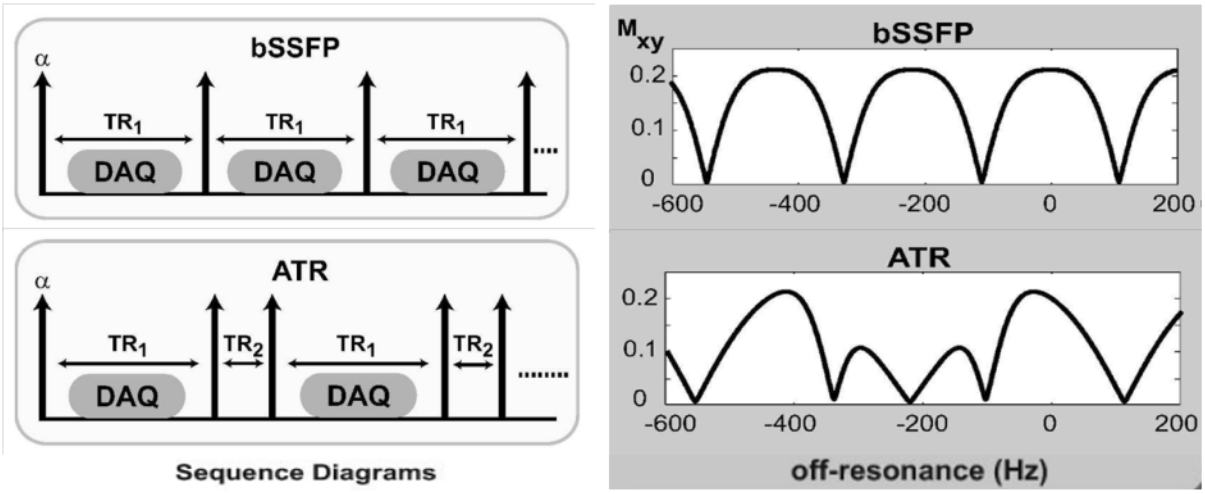

Figure 1.2 Conventional and FS-ATR SSFP pulse sequences and their corresponding transverse magnetization profiles are shown above. All RF pulses have the same flip angle (α) and RF phase-cycling pattern (0-180o). ATR-SSFP creates a wide stop-band around the fat resonance (220 Hz at 1.5T).

Alternating repetition times and RF-pulse phase in bSSFP sequence change the periodicity of the frequency response profile and width of pass and stop bands (32). A pulse sequence diagram of alternating repetition times SSFP (ATR-SSFP) and its corresponding magnetization profile is shown in Figure 1.2 along with the conventional SSFP sequence. The ATR-SSFP sequence uses two separate TRs, TR1 and TR2, and two RF excitations, RF1 and RF2. Data acquisition occurs only during TR1, while RF2 and TR2 are used to change the shape of the frequency response to create a stopband at the frequency of fat. RF1 and RF2 have the same flip angle. Compared to regular SSFP, ATR-SSFP adds a wide stopband at the center of every other passband as seen in Figure 1.2. Fat suppression can be achieved if the separation between this stopband and center of the passband is equal to 1/(TR1 + TR2). The phase of RF2 can be calculated from the following equation

$$\Psi_2 = 360^o \, \tau \, /(1+ \tau)$$

Where $\tau = TR_2 / TR_1$

The LC-SSFP technique requires sampling k-space twice with the RF phase alternating by π radians each TR in the first pass and remaining constant in the second pass. Due to off-resonance excitation, LC-SSFP requires a large phase correction to achieve coherent combination of the water signal between the dual half-echoes within each TR. In contrast, the 3D radial FS-ATR sequence provides fat suppression with a single k-space acquisition that is not dependent upon a phase correction, as water is imaged on-resonance.

We have combined the multi-acquisition fat-water separation ATR-SSFP sequence with the previously described 3D VIPR trajectory for ultra-high isotropic resolution research studies (35).

1.3 Ultra Short Echo Time Imaging

1.3.1 Two-Dimensional Radial Ultra-short Echo-Time Imaging

Shorter echo times (TEs) can be achieved by using half radio-frequency (rf) excitations and radial imaging. In the ultrashort TE (UTE) approach, half-sinc RF excitation pulses are used to achieve ultrashort echo times in the range of 0.03-0.2 ms (36)(37). When a slice selective gradient is used with conventional 2DFT imaging, a delay for a refocusing gradient between the RF excitation and data acquisition is necessary to rephase the signal. To avoid the need for a rephasing gradient in UTE imaging, k-space data is acquired twice with opposing slice selective gradient polarity. These two acquisitions are then combined to generate signal confined primarily from the desired slice (36). A typical UTE pulse sequence diagram is shown in Figure 1.3. After adding these two acquisitions, the signal is selectively in phase as with conventional 2DFT. In addition to the specialized RF pulse, the TE time is further reduced by eliminating the time

required for phase encoding by using a 2D radial sampling of k-space. So, in UTE sequence, data sampling can begin as soon as the RF pulse and the slice selection gradient are ramped down to zero, therefore the echo time is limited only by the hardware switching time.

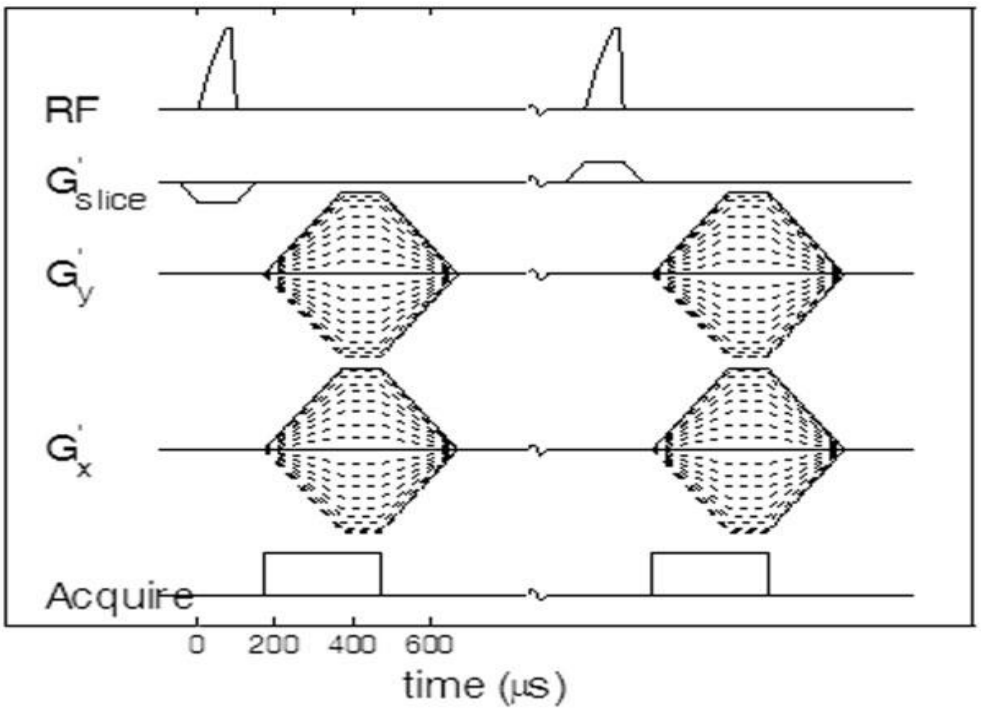

Figure 1.3 Pulse sequence diagram for a basic UTE sequence. The half RF pulse is applied with a negative slice select gradient first and repeated with a positive slice select gradient. Data acquisition starts immediately as the slice select gradient ramp down to zero.

1.3.2 Three-Dimensional Radial Ultrashort Echo-Time Imaging

Alternatively, UTE imaging can be performed using a 3D technique that employs a nonselective RF excitation with 3D radial FID sampling, yielding image data with isotropic spatial resolution (38)(39)(40). Using this approach, the RF excitation is more robust and of shorter duration, thereby minimizing T2 decay during excitation. In contrast to 2D UTE technique, 3D UTE

approach requires only one excitation pre K-space trajectory and hence reduced scan time. The basic pulse sequence for 3D radial UTE imaging is shown in Figure 1.4. A rectangular radiofrequency (RF) excitation block pulse with duration TRF is followed by 3D centric radial sampling of the k-space data (TAQ) after echo time TE. As in 2D UTE sequence, effective TE is defined as the interval between the end of RF excitation and the start of the readout gradient.

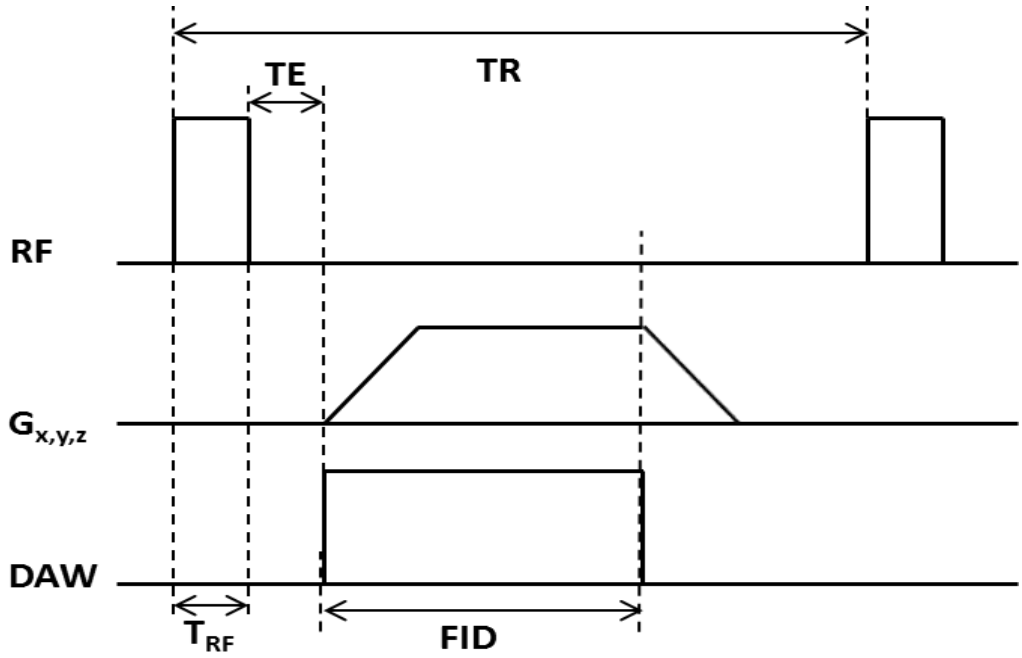

Figure 1.4 Three-dimensional UTE sequence. A short-duration hard radiofrequency (RF) pulse is followed by 3D radial FID ramp sampling during data acquisition period TAQ.

1.4 IDEAL Fat/Water Decomposition

In Magnetic Resonance (MR) imaging, in vivo MR images usually contains signal from both water and fat protons. In many applications, contribution from water signal is of the primary

interest. However, fat signal appears bright in many pulse sequences and obscures the water signal(41). Fat suppression is commonly used in MR imaging to suppress fat signal and improve underlying lesion conspicuity.

Many methods have been developed to suppress fat signal in MR imaging. Fat saturation during excitation have been achieved using spectrally selective pulses that excites fat only (based on the difference in the resonance frequencies of water and fat protons) followed by a spoiling gradient to diphase the lipid signal before water excited for imaging (42,43). On the other hand, Inversion recovery imaging used to null fat signal(44). In this method, an inversion pulse is first applied to flip fat and water magnetization by 180^{o} and then both allowed relaxing back to the magnetic field direction. When fat longitudinal magnetization reach the null point before water because of its short T_1 relaxation time, water is excited for imaging.

Dixon(45), used spectroscopic imaging to separate fat and water through postprocessing. The Dixon technique is based on the chemical shift difference between fat and water. The two point Dixon method(45) uses a dual echo acquisition to separate fat and water. It acquires two complex images with a (0, 180^{o}) sampling strategy where fat and water signal in phase in one image and out of phase in the other image. separated fat and water images achived by adding and subtracting these two complex images. However, in the presence of field inhomogeneties, phases from the two echo images differ than expected and signal from fat and water is mixed. Three point Dixon technique(46–48) acquires three complex images at three different echo times and solve for field inhomogeneties information in addition to fat and water. This method requires specific echo spacing which can be difficult to reconcile with other timing requirements.

Reeder(41,49) further refined this approach in 2004 with the use of arbitrary and unequaly spaced echoes and maximized noise performance of the fat-water decomposition. Iterative

decomposition of Water and Fat with Echo Asymmetry and Least Squares Estimation (IDEAL) (49) is a multi-echo chemical species separation technique which has been shown to effectively separate water and fat with a number of different acquisitions(49)(50)(51). In IDEAL, the B0 inhomogeneity map is iteratively solved by minimizing the residue of the signal model and acquired images. With a known chemical shift between species of interest, the signal equations for a series of echo times provide a linear system of complex equations. Because of the presence of B0 inhomogeneity, n + 1 signal measurements are required where n is the number of chemical species to be resolved. The multi species signal is modeled as :

$$\hat{s}_n = \hat{s}_n^R + i s_n^I = \sum_{j=1}^{M} \left(\rho_j^R c_{jn} - \rho_j^I d_{jn} \right) + i \sum_{j=1}^{M} \left(\rho_j^R d_{jn} + \rho_j^I c_{jn} \right)$$

in which ρ_j^R and ρ_j^I are the real and imaginary components of the jth chemical species(49).

Chapter 2:

Rapid Isotropic Resolution Cartilage Assessment Using Radial FS-ATR bSSFP Imaging

First we concentrate on needs for whole organ assessment in longitudinal studies. Most MR sessions in longitudinal studies are limited to 30 minutes. All of these studies require assessment of all joint structures so pain from other damage to ligaments, tendons, and menisci is not improperly attributed to cartilage degeneration. This task is referred to as Whole Organ Assessment. Any time not devoted to Whole Organ Assessment, a largely morphological imaging task, can be devoted to new cutting edge methods assessing cartilage changes prior to volume loss.

This chapter focuses on rapid whole organ assessment by producing high resolution, volumetric scans of the entire knee joint that can assess all structures. Meanwhile, their high isotropic resolution allows one to track cartilage volume changes with increased sensitivity to smaller changes. The sensitivity to small changes ultimately makes longitudinal trials of new treatments shorter, requires fewer subjects, and requires less cost.

2.1 Introduction[1]

High resolution magnetic resonance (MR) imaging techniques play an important role in evaluating the articular cartilage of the knee joint. High resolution images allow for early detection of cartilage lesions in symptomatic patients (52) and provide more accurate cartilage volume analysis in osteoarthritis research studies (53). Three-dimensional sequences are superior to two-dimensional sequences for high resolution cartilage imaging due their improved signal-to-noise ratio (SNR) efficiency and ability to acquire thin continuous slices through joints (54–56). Various three-dimensional sequences have been used to evaluate articular cartilage including gradient-echo sequences with dark synovial fluid (57) and bright synovial fluid (58), dual-echo in the steady-state (DESS) (59), driven equilibrium fourier transform (DEFT) (60), fast spin-echo sequences (61), and balanced steady-state free-precession (bSSFP) sequences (62,63). Fat suppression is typically added to these sequences to optimize the dynamic contrast range of the image, reduce chemical shift artifact, and improve the detection of subchondral bone marrow edema which is an important secondary sign of cartilage degeneration. The fact that so many fat-suppressed three-dimensional cartilage imaging techniques exist illustrates the inherent limitations of each imaging strategy.

bSSFP sequences in particular offer many advantages for evaluating articular cartilage. The sequences have high SNR efficiency and produce images with bright synovial fluid and excellent tissue contrast (54,55,63). Various methods have been used to suppress fat signal on bSSFP images, but all currently used techniques have limitations. Frequency selective fat-suppressed

[1] This chapter has been accepted in the Journal of Magnetic Resonance Imaging and published first online in October of 2013.

bSSFP sequences periodically interrupt the steady-state to saturate fat spins, but the fat signal is partially restored during each imaging interval (64). Water excitation bSSFP sequences effectively suppress fat signal but require long repetition times (TR) which lead to off resonance banding artifacts in areas of magnetic field inhomogeneity (65). Fluctuating equilibrium magnetic resonance (FEMR) (66) and linear combination (LC) bSSFP (67) sequences separate fat and water signal without a loss in SNR efficiency, but the optimal TR needed for successful implementation at 3.0T allows little time for spatial encoding and thereby limits spatial resolution. Moreover, LC-SSFP spectral response shows a pass-band width of 1/2TR as compared to 1/TR for conventional SSFP.

Alternating repetition time (ATR) methods have been developed for bSSFP imaging to create more time for spatial encoding while maintaining a short TR and thereby minimizing off resonance banding artifacts. Wideband bSSFP utilizes ATR to create a steady-state with a pass-band 1.5 times wider than the pass-band of conventional bSSFP which reduces banding artifacts but provides no fat-suppression (68). Leupold and associates described a method which combines radiofrequency (RF) phase cycling with ATR to provide fat-suppression for bSSFP imaging at 3.0T. The technique uses one broad stop-band and three pass-bands at a TR_1:TR_2 ratio of 1:3 with a 3.6 ms encoding time and a TR of 4.6 ms to create a stop-band at 440 Hz to suppress fat signal. However, most ATR methods of fat-suppression have been demonstrated with spatial resolution at or just below 1mm as their use of Cartesian k-space trajectories require spatial pre-encoding and rewinding pulses which reduces data acquisition time (32).

A new bSSFP technique called Radial-ATR has been recently developed which combines ATR fat-suppression with a three-dimensional radial k-space trajectory and addresses many of the challenges associated with high resolution fat-suppressed bSSFP imaging (34). The radial k-space trajectory requires no phase encoding, slice encoding, or dephasing gradients which optimizes data acquisition, shortens the TR, and allows high isotropic resolution fat-suppressed images to be acquired with minimal off-resonance banding artifacts. By using the three-dimensional radial k-space trajectory, almost the entire TR can be utilized to acquire data which provides significantly higher resolution than a Cartesian trajectory within the constrained TR. (30). This study was performed to compare the SNR efficiency of Radial-ATR with other fat-suppressed three-dimensional cartilage imaging sequences and to determine the feasibility of using radial-ATR for high resolution cartilage imaging of the knee joint at 3.0T.

2.2 Materials and Methods

2.2.1 Description of Radial−ATR Sequence

Radial−ATR is a bSSFP sequence which produces fat suppressed three-dimensional images of the knee joint with T1/T2 tissue contrast and high isotropic resolution. The sequence utilizes a three-dimensional out-and-back radial k-space trajectory which allows for almost continuous acquisition of image data (30). Fat-suppression is achieved using an ATR method in which two different alternating length TRs (TR1 and TR2) and RF phase cycling is used to shape the spectral frequency response to place a stop-band over the fat resonance (32).

Radial-ATR uses a thick slab-select excitation to reduce slab refocusing time and a dual half-echo trajectory within a single TR (=TR1 + TR2). The radial trajectory requires no phase encoding or slice encoding since data acquisition begins and ends at the *k*-space origin. The thick slab selection and absence of phase encoding, slice encoding, or dephasing gradients shortens the TR and limits off-resonance banding artifacts. By using the three-dimensional radial k-space trajectory, almost the entire TR can be utilized to acquire data which provides significantly higher resolution than a Cartesian trajectory within the constrained TR. For the TR_1 of 3.45ms needed for optimal fat-suppression using the ATR method at 3.0T, the maximum achievable isotropic resolution with a radial trajectory is 0.3mm as compared to 0.5mm with a Cartesian trajectory (30). Corrections are made for deviations of the radial k-space trajectory due to eddy current effects and anisotropic gradient delays by spatially encoding a thin test slice with a bipolar gradient pulse and analyzing the resulting phase (35).

While Radial-ATR extends the TR for spatial encoding at 3.0T, a 3.6ms encoding time and a TR of 4.6ms is needed for optimal fat-suppression using the ATR method (32). Consequently, TR1 and TR2 are chosen to be 3.45ms and 1.15ms respectively with the phase of the second RF pulse shifted 180° with respect to the first RF pulse. When combined with conventional 0°-180° bSSFP phase cycling, a 0°-180°-180°-0° cycle is generated that repeats every four RF pulses. This phase cycling scheme centers the fat signal on the stop-band of the frequency response (32).

Radial−ATR uses a 4.6 ms TR (TR1=3.45 ms and TR2=1.15 ms), 15° flip angle, 0.3 ms and 1.8 ms TE for the first and second half-echo respectively, ±125 kHz bandwidth, and one signal

average. Using a 15 cm field of view (FOV) and either a 256 x 256, 384 x 384, or 512 x 512 matrix, Radial−ATR produces fat-suppressed three-dimensional images of the knee joint with 0.6 mm and 0.4 mm isotropic resolution in 5 minutes and 0.3 mm isotropic resolution in 8 minutes.

2.2.2 Study Group

The study was performed in compliance with Health Insurance Portability and Accountability Act (HIPAA) regulations and with approval from our institutional review board. All subjects signed written informed consent prior to participation in the study. All subjects underwent an MR examination of the knee using the same 3.0T scanner (Discovery MR750, GE Healthcare, Waukesha, WI; maximum gradient strength of 50 mT/m and maximum slew rate of 200 $mT \cdot m^{-1} \cdot sec^{-1}$) and an 8-channel phased-array extremity coil (Precision Eight TX/TR High Resolution Knee Array; In Vivo, Orlando, FL).

A study group consisting of 5 asymptomatic volunteers (4 males and 1 female with an age range between 23 years and 28 years and an average age of 26.6 years) was used to compare the SNR performance of Radial-ATR with other fat-suppressed three-dimensional cartilage imaging sequences. All subjects underwent an MR examination of both knees consisting of double acquisition sagittal Radial-ATR, three-dimensional fast spin-echo (FSE-Cube), three-dimensional gradient recall-echo acquired in the steady-state (GRASS), and three-dimensional spoiled gradient recall-echo (SPGR) sequences with the double acquisition of each sequence performed one immediately following the other.

Table 2.1: Acquisition parameters for the three-dimensional cartilage imaging sequences

Imaging Parameter	Radial-ATR	FSE-Cube	GRASS	SPGR
TR (ms)	4.6	2217	12.4	12.4
TE (ms)	0.3/1.8	23.6	3.4/4.2/5.0	3.4/4.2/5.0
Flip Angle (deg)	15	90	50	14
Bandwidth (kHz)	125	31.2	31.2	31.2
Field of View (cm)	15	15	15	15
Matrix	256 x 256	256 x 256	384 x 224	384 x 224
Slice Thickness (mm)	0.6	0.6	1.0	1.0
In-Plane Resolution (mm)	0.6 x 0.6	0.6 x 0.6	0.4 x 0.7	0.4 x 0.7
Voxel Volume (mm3)	0.22	0.22	0.28	0.28
Number of Slices	256	392	84	84
Scan Time (min)	5	5	5	5

The sequences used the imaging parameters summarized in Table 2.1 and were optimized to produce 0.6 mm isotropic resolution images of the knee joint, or as close as possible, in a 5 minute scan time (58)(69). FSE-Cube, GRASS, and SPGR utilized autocalibrating reconstruction for cartesian sampling (ARC) for parallel imaging. FSE-Cube used a spectral inversion recovery pulse for fat-suppression, while GRASS and SPGR used a chemical shift fat-water separation method called iterative decomposition of water and fat with echo asymmetry and least-squares estimation (IDEAL) (70). In order to compare tissue contrast of bSSFP

sequences with and without fat-suppression, double acquisition VIPR-ATR and non-fat-suppressed radial bSSFP (Radial-bSSFP) sequences were also performed one immediately following the other on a single 27 year male asymptomatic volunteer. The radial-bSSFP sequence used the same radial k-space trajectory as Radial-ATR and was acquired with TR of 2.9 ms, TE of 0.5 ms, 15^{o} flip angle, 125 kHz bandwidth, 15 cm field of view, 256 x 256 matrix, 0.6mm slice thickness, 256 slices, and 5 minute scan time.

A second study group consisting of 7 asymptomatic volunteers (3 males and 4 females with an age range between 23 years and 28 years and an average age of 25.4 years) and 3 patients with Kellgren-Lawrence grades 1 or 2 knee osteoarthritis (2 males and one female with an age range between 46 years and 52 years and an average age of 48.0 years) was used to determine the feasibility of Radial-ATR for performing high resolution cartilage imaging of the knee joint. All subjects underwent an MR examination of the knee consisting of sagittal 0.4 mm isotropic resolution Radial-ATR, 0.3 mm isotropic resolution Radial-ATR, FSE-Cube, GRASS, and SPGR sequences. The imaging parameters of all sequences were identical to those summarized in Table 1 except that 0.4 mm isotropic resolution Radial-ATR used a 384 x 384 matrix, 0.4 mm x 0.4 mm in-plane resolution, 0.4 mm slice thickness, and 5 minute scan time and 0.3 mm isotropic resolution Radial-ATR used a 512 x 512 matrix, 0.3 mm x 0.3 mm in-plane resolution, 0.3 mm slice thickness, and 8 minute scan time.

2.2.3 Image Analysis

The MR examinations of subjects in the first study group were used to compare SNR performance of the three-dimensional sequences. All images were up-sampled by SINC interpolation to get the same display matrix. Addition and subtraction images for each sequence were created using Image J software (http://imagej.nih.gov/ij/, 1997-2012). The SNR of cartilage, synovial fluid, and bone marrow and the contrast-to-noise ratio (CNR) between cartilage and synovial fluid and between cartilage and bone marrow were calculated using a double acquisition method previously described for parallel imaging techniques (71). Regions of interests (ROIs) containing 20 pixels for cartilage and synovial fluid, 50 pixels for bone marrow, and 200 pixels for muscle were placed at identical locations on the addition and subtraction images for all sequences. Signal was defined as the average signal within the ROI in cartilage, synovial fluid, and bone marrow on the addition images, while noise was defined as the standard deviation of the signal within the ROI in muscle on the subtraction images. The ROI in muscle was placed at a location where motion, pulsation, or aliasing artifact would not influence the stochastic noise measurement. SNR and CNR values were calculated using the following equations:

Equation 1: $$SNR = \frac{Signal}{Noise}$$

Equation 2: $$CNR = \frac{|Signal\ Tissue\ 1 - Signal\ Tissue\ 2|}{Noise}$$

Mann-Whitney Wilcoxon tests were used to compare SNR and CNR between sequences with differences considered statistically significant for p-values less than 0.05.

The MR examinations of subjects in the second study group were evaluated independently by two fellowship-trained musculoskeletal radiologists (authors H.G.R. and K.S.L.) with 4 and 6 years of clinical experience to determine whether Radial-ATR could be used for high resolution cartilage imaging. The radiologists assessed the 0.3 mm and 0.4 mm isotropic resolution Radial-ATR sequences based upon the following four qualitative measures of image quality: tissue contrast, clarity of articular surface, cartilage lesion conspicuity, and artifacts. A four-level scale was used for qualitative assessment in which a score of 4 indicated excellent image quality, a score of 3 indicated good image quality, a score of 2 indicated acceptable image quality, and a score of 1 indicated poor image quality (72).

2.3 Results

Comparison Radial-ATR, FSE-Cube, GRASS, and SPGR images of the knee joint with similar voxel volumes and identical scan times are shown in Figure 2.2. Average SNR values for cartilage, synovial fluid, and bone marrow were 54.7, 153.3, and 12.9 respectively for Radial ATR, 30.8, 44.1, and 1.9 respectively for FSE-Cube, 13.3, 46.9, and 3.3 respectively for GRASS, and 19.1, 8.1, and 2.1 respectively for SPGR. Average CNR values between cartilage and synovial fluid and between cartilage and bone marrow were 98.6 and 41.8 respectively for VIPR-ATR, 13.4 and 28.8 respectively for FSE-Cube, 33.6 and 10.0 respectively for GRASS, and 11.0 and 16.9 respectively for SPGR.

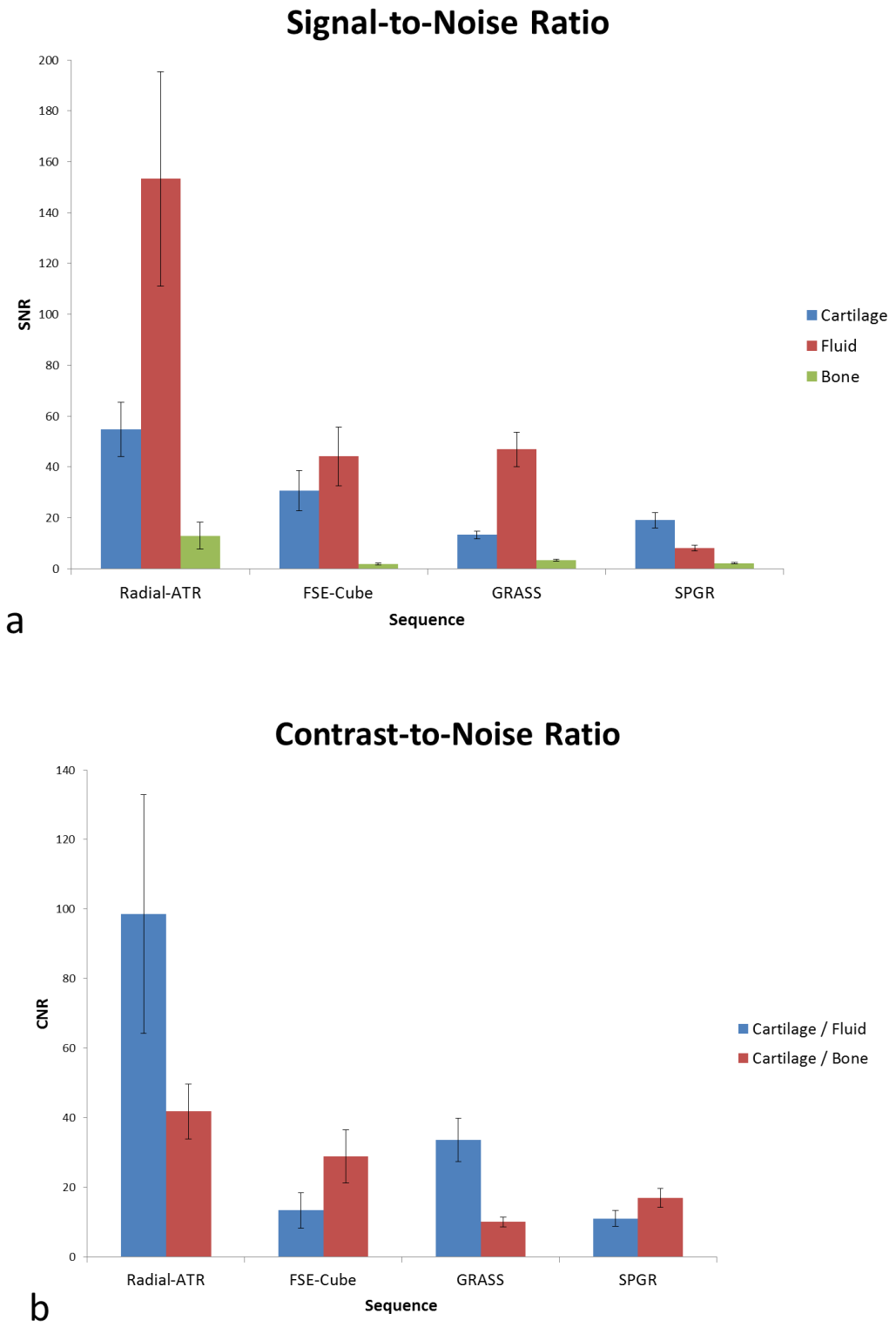

Figure 2.1 Comparison of (a) SNR and (b) CNR for the three-dimensional cartilage imaging sequences.

Radial-ATR had significantly higher ($p<0.001$) SNR of cartilage and synovial fluid than FSE-Cube, GRASS, and SPGR. However, Radial-ATR also had significantly higher ($p<0.001$) SNR of bone marrow than the other sequences indicating decreased ability to suppress fat signal (Figure 2.1a). Radial-ATR had significantly higher ($p<0.001$) CNR between cartilage and synovial fluid and significantly higher ($p<0.01$) CNR between cartilage and bone marrow than FSE-Cube, GRASS, and SPGR (Figure 2.1b).

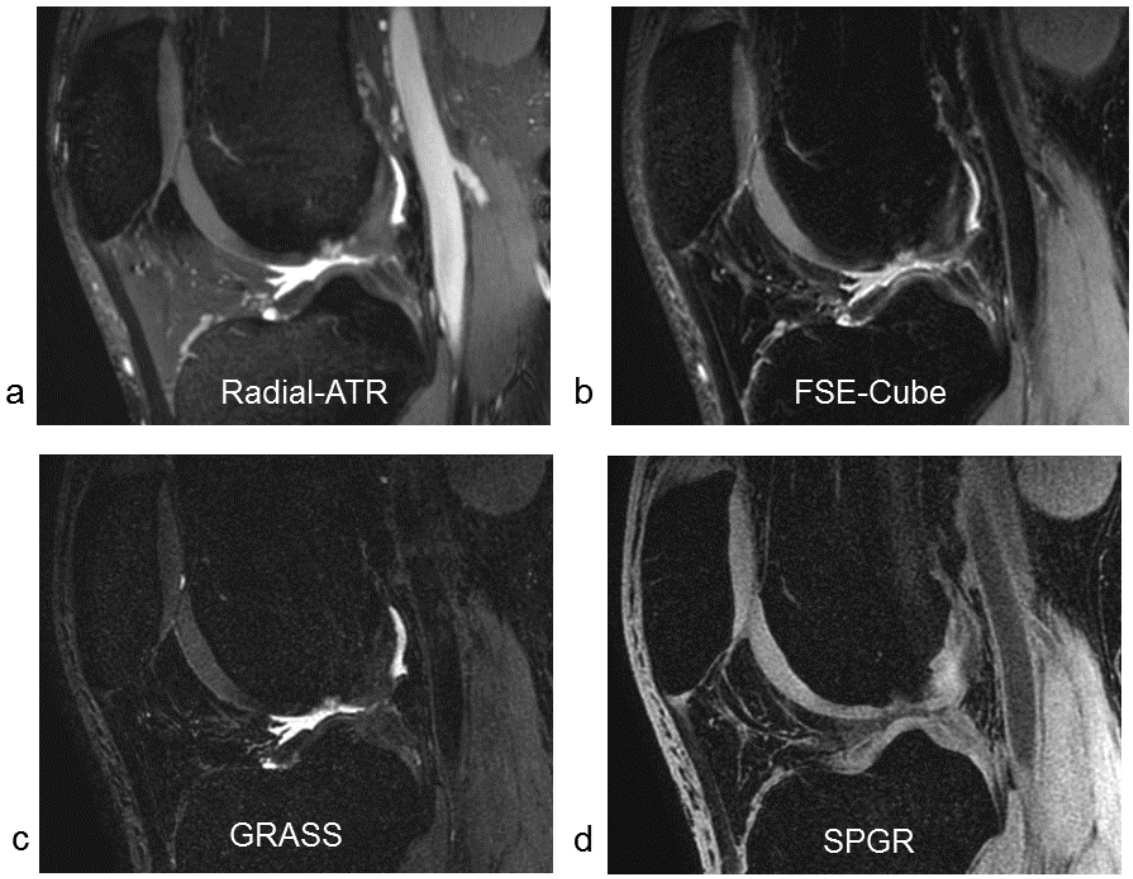

Figure 2.2 Sagittal (a) Radial-ATR, (b) FSE-Cube, (c) GRASS, and (d) SPGR images of the knee joint with similar voxel volumes and identical scan times in a 25 year old male asymptomatic volunteer.

Comparison Radial-ATR and Radial-bSSFP images of the knee joint with identical voxel volumes and scan times are shown in Figure 2.3. SNR values for cartilage, synovial fluid, and bone marrow were 51.2, 146.5, and 14.7 respectively for Radial ATR and 70.4, 95.7, and 97.5 respectively for radial-bSSFP. CNR values between cartilage and synovial fluid and between cartilage and bone marrow were 95.3 and 36.5 respectively for VIPR-ATR and 25.3 and 27.1 respectively for radial-bSSFP.

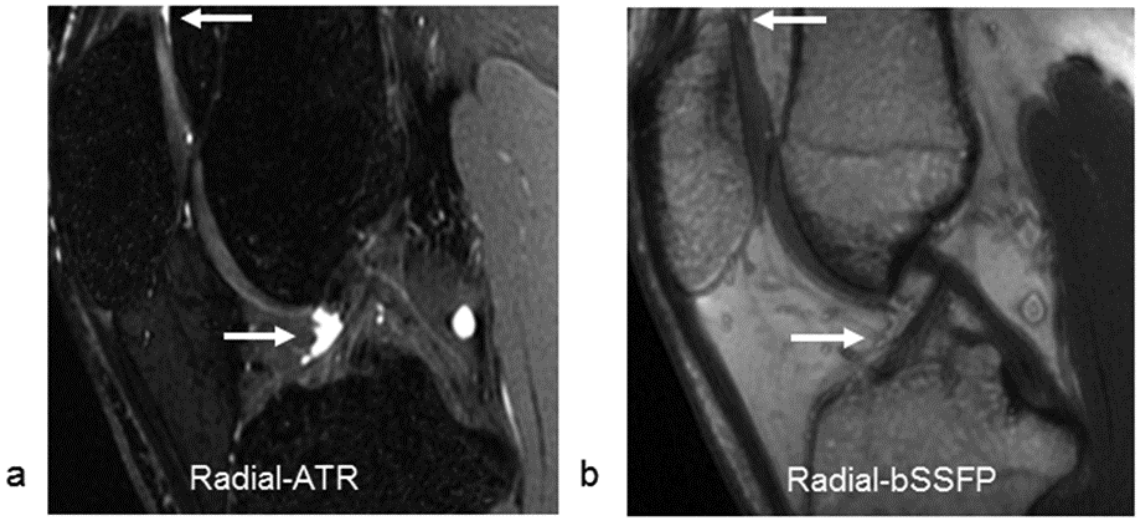

Figure 2.3 Sagittal (a) Radial-ATR and (b) Radial-bSSFP images of the knee joint with similar voxel volumes and identical scan times in a 27 year old male asymptomatic volunteer. Note the high contrast between synovial fluid (arrows) and adjacent cartilage and fat on the Radial-ATR image. The synovial fluid (arrows) on the Radial-bSSFP image cannot even be visualized since it has almost identical signal intensity as adjacent fat.

The 0.3 mm and 0.4 mm isotropic resolution Radial-ATR sequences received high scores from both radiologists for all four qualitative measures of image quality. The average score for tissue contrast, clarity of articular surface, cartilage lesion conspicuity, and artifacts were 4.0, 3.8, 3.8, and 4.0 respectively for 0.4 mm isotropic resolution VIPR-ATR and 4.0, 4.0, 4.0, 4.0, and 4.0 respectively for 0.3 mm isotropic resolution VIPR-ATR. The high in-plane spatial resolution, thin slices, excellent tissue contrast, and absence of blurring on Radial-ATR images resulted in increased clarity and sharpness of the articular surface and excellent visualization of cartilage lesions (Figure 2.4).

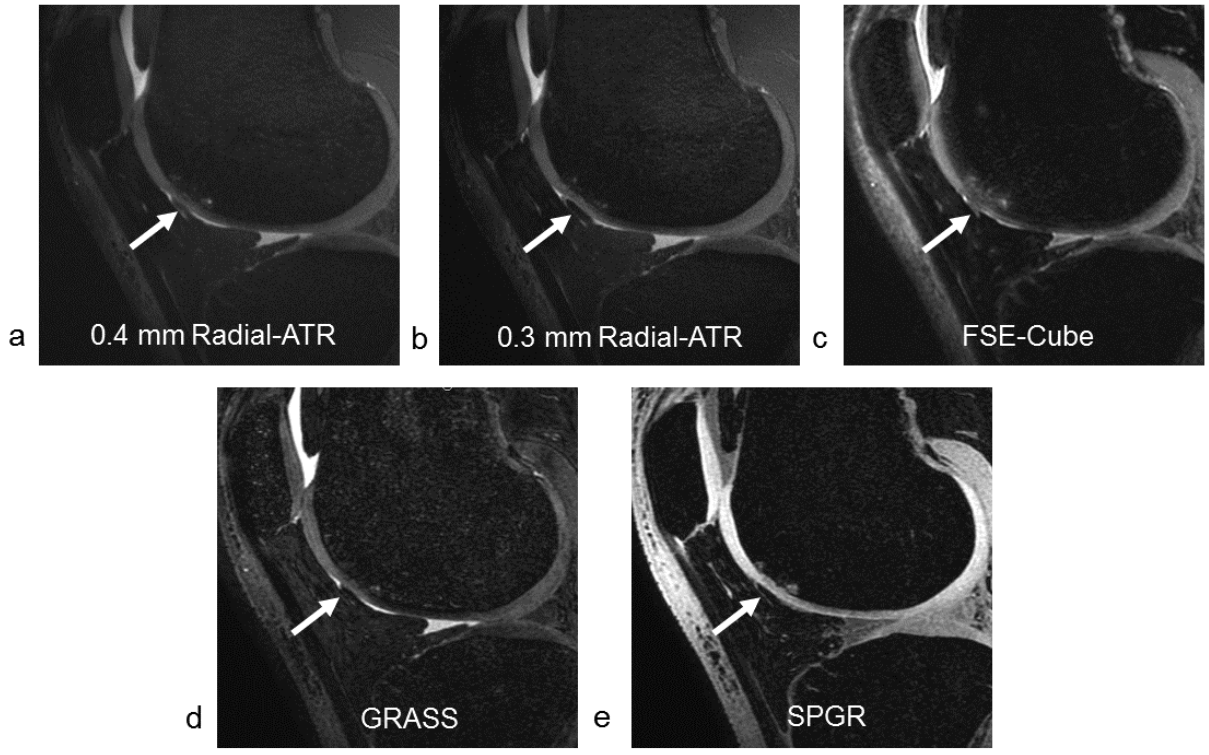

Figure 2.4 Sagittal (a) 0.4 mm isotropic resolution Radial-ATR, (b) 0.3 mm isotropic resolution Radial-ATR, (c) FSE-Cube, (d) GRASS, and (e) SPGR images of the knee joint in a 51 year old male patient with osteoarthritis show a partial-thickness cartilage lesion on the femoral trochlea (arrows).

Radial-ATR was also able to detect other joint pathology in patients with knee osteoarthritis including meniscal and ligament tears, tendinopathy, and subchondral cysts (Figure 2.5). No degradation of image quality due to off-resonance banding artifacts was noted.

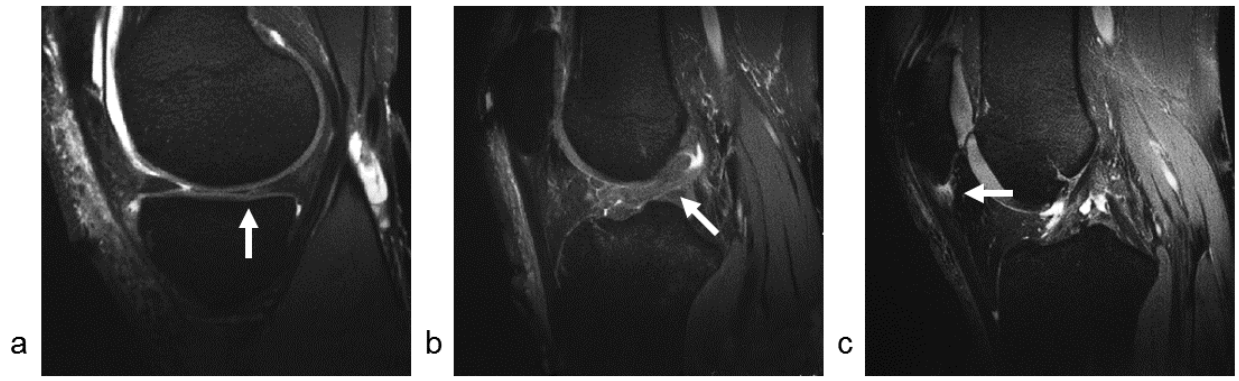

Figure 2.5 (a and b) Sagittal 0.3 mm isotropic resolution Radial-ATR images of the knee joint in a 51 year old male patient with osteoarthritis show a posterior horn medial meniscus tear (arrow in a) and anterior cruciate ligament tear (arrow in b). (c) Sagittal 0.3 mm isotropic resolution Radial-ATR image of the knee joint in a 46 year old male patient with osteoarthritis shows patellar tendinopathy (arrow).

2.4 Discussion

Radial-ATR acquired fat-suppressed three-dimensional images of the knee joint at 3.0T with 0.4 mm to 0.6 mm isotropic resolution in 5 minutes and 0.3 mm isotropic resolution in 8 minutes. The fat-suppression of Radial-ATR provided superior tissue contrast when compared to a non-fat-suppressed bSSFP sequence using a similar radial k-space trajectory. The isotropic source data could be used to create multi-planar Radial-ATR reformat images which allowed articular cartilage to be evaluated in any orientation following a single acquisition. Radial-ATR

compared favorably with other fat-suppressed three-dimensional sequences for evaluating the articular cartilage of the knee joint at 3.0T.

Radial-ATR had significantly higher cartilage and synovial fluid SNR than FSE-Cube, GRASS, and SPGR sequences with similar voxel volumes and identical scan times. The higher SNR of Radial-ATR when using identical scan times as the other cartilage imaging sequences was likely due to its radial k-space trajectory. Radial-ATR requires no phase encoding, slice encoding, or dephasing gradients which allows for nearly continuous acquisition of image data (30). The more efficient k-space trajectory allowed Radial-ATR to acquire higher isotropic resolution images of the knee joint at 3.0T in identical or shorter periods of time than Cartesian-based fat-suppressed three-dimensional cartilage imaging sequences currently available on both GE Healthcare (69) and Siemens (73) MR platforms. Radial-ATR images were not degraded by off-resonance banding artifacts, which commonly occur when using other fat-suppressed bSSFP sequences, due to its ability to maintain a short TR at high isotropic resolutions.

One limitation of Radial-ATR for evaluating articular cartilage is its suboptimal fat-suppression. Radial-ATR had significantly higher bone marrow SNR than FSE-Cube, GRASS, and SPGR sequences indicating a decreased ability to suppress fat signal. The frequency selective stop-band placed over the fat resonance on Radial-ATR has a significant ripple which may not remove all fat signal from the image (32). Thus, it is not surprising that Radial-ATR had higher bone marrow SNR than FSE-Cube which used a spectral inversion recovery pulse and GRASS and SPGR which used a chemical shift fat-water separation method. Despite its decreased ability to suppress fat signal, Radial-ATR had greater CNR between cartilage and bone marrow than the

other sequences which can be attributed to its much higher cartilage SNR. Nevertheless, the reduced fat-suppression of Radial-ATR may decrease its sensitivity for detecting bone marrow edema lesions and subchondral cysts in patients with osteoarthritis. We are currently investigating modifications in design parameters of Radial-ATR such as changes in the TR1:TR2 ratio and the order in which TR1 and TR2 are interleaved which may reduce the ripple in the fat stop-band and thereby improve fat-suppression. Additional modifications of the ATR technique have also been described to provide improved fat-suppression for bSSFP imaging. Cukur and associates described a multiple acquisition ATR method for fat-water separation using in-phase and out-of-phase bSSFP images (74). Lee and associates used a single acquisition multiple TR method to create a wider stop-band over the fat frequency which provided improved fat-suppression at the cost of reduced SNR efficiency and increased scan time (75).

Vastly undersampled isotropic steady-state free-precession (VIPR-SSFP) is another bSSFP sequence which uses a radial k-space trajectory to produce fat-suppressed images of the knee joint with 0.4 mm isotropic resolution in 5 minutes (35). Previous studies have shown favorable comparisons between VIPR-SSFP and other two-dimensional and three-dimensional cartilage imaging sequences at 3.0T (35,69). However, VIPR-SSFP utilizes a linear combination fat-water separation method which requires two k-space acquisitions and places the center frequency halfway between fat and water resonances. VIPR-SSFP also uses a point- by-point phase correction to avoid blurring as water accrues a phase shift over the out and back trajectory. The need for VIPR-SSFP to image off-resonance ultimately results in image blurring and suboptimal fat-suppression at isotropic resolutions higher than 0.4 mm. Since Radial-ATR is acquired on the water resonance, there are no resolution dependent effects on imaging blurring or fat-

suppression and no need for point-by-point phase correction. In addition, Radial-ATR requires only a single k-space acquisition which allows more unique radial projects to be obtained in the same scan time which reduces undersampling artifact.

Our study had several limitations. One limitation was that Radial-ATR was not compared to all currently used three-dimensional cartilage imaging sequences including DESS, true fast imaging with steady-state precession (true-FISP), and sampling perfection with application oriented contrasts using different flip angle evolutions (SPACE) (73). However, many of the sequences used in cartilage comparison studies are available only on certain MR vendor platforms, and thus it would be difficult to directly compare all three-dimensional cartilage imaging sequences in a single study. Another limitation of our study was that the Radial-ATR was only used to evaluate a small number of patients with osteoarthritis. However, the objective of this study was merely to compare the SNR performance of Radial-ATR with other three-dimensional sequences and to document the feasibility of using Radial-ATR for high resolution cartilage imaging. Larger clinical studies with surgical correlation are needed to better assess the ability of Radial-ATR to detect cartilage lesions and other joint pathology in patients with osteoarthritis. A final limitation of our study was that the SNR of cartilage, synovial fluid, and bone marrow could not be calculated using noise measurements obtained separately in each individual tissue. Measuring noise in small ROIs placed in cartilage and synovial fluid utilizing the double acquisition method is prone to error due to the small number of pixels used for noise measurements and imperfect co-registration of subtraction images (69). Thus, we felt that using the standard deviation of signal on the subtraction images in a large ROI placed at identical

locations in muscle, which appears homogenous on all sequences, would provide the most accurate assessment of image noise.

2.5 Conclusion

In conclusion, Radial-ATR produced multi-planar fat-suppressed images of the knee joint with high isotropic resolution which provide excellent visualization of the articular cartilage of the knee joint at 3.0T. Radial-ATR had higher cartilage and synovial fluid SNR than FSE-Cube, GRASS, and SPGR sequences with similar voxel volumes and identical scan times. The improved SNR efficiency allowed Radial-ATR to acquire higher isotropic resolution images of the knee joint than other currently available fat-suppressed three-dimensional cartilage imaging sequences with no image degradation due to off-resonance banding artifacts (69)(73). Due to its highly versatile bSSFP tissue contrast (62)(76), Radial-ATR may also be useful for evaluating the menisci, ligaments, bone marrow, and other joint structures which can be sources of pain in patients with osteoarthritis. Additional studies are needed to determine whether Radial-ATR can be used to detect early cartilage degeneration in clinical practice and to provide rapid "whole-organ" joint assessment and cartilage volume analysis in osteoarthritis research studies.

Chapter 3:

High Contrast 3D IDEAL Ultrashort TE (UTE) Imaging

Nuclear magnetic resonance (NMR) spectroscopy has identified three exchangeable water components within cartilage: bulk water loosely bound to the macromolecular matrix (W_{BW}), water tightly bound to proteoglycan (W_{PG}), and water tightly bound to collagen (W_{COL}). Considerable efforts are being placed already on the difficult problem of fitting the rapidly decaying W_{COL} signal using trains of gradient echoes. These methods use a multi-shot approach to image several echos about echo times of interest and thus require such long scan times that they are often performed on ex-vivo tissue(77)(78)(79)(80)(81)(82).

The previous chapter used bSSFP methods that were sensitive to the W_{PG}, W_{BW}, and synovial fluid compartments. This chapter discusses in a method to assess the W_{COL} component through altering the IDEAL model. It is much more robust to B0 inhomogeneity than the subtraction method and takes considerably less time than fully mapping the UTE components quantitatively, which often takes an hour on ex-vivo samples. Though the proposed method is not quantitative, it provides rapid high resolution estimation of the ultrashort echo components throughout joint in-vivo in a reasonable scan time of 10 minutes.

The method has applications beyond the musculoskeletal system for segmenting tissue for MR-based PET attenuation correction. The application allows the segmentation of fat, water, and bone tissue in a reasonable scan time. An example of its capability in the thorax is provided.

3.1 Introduction

A vast number of clinically relevant tissues exhibit extremely short transverse relaxation times (T2 or T2*). This is especially true for muscular skeletal (MSK) tissues, including calcified cartilage and bone, tendons, the knee meniscus, cortical bone, and ligaments, all of which short T2 components (83). Unfortunately, the MR signal of these tissues significantly decays before conventional imaging sequences complete signal acquisition rendering them invisible and can only be appreciated when traumatic damage alters the local cellular environment (e.g. edema) (84)(85). However, the ability to visualize subacute changes in these tissues has important implications for offering assessment of subacute injury and pathogenesis of degenerative disease(37). Several investigations methods have been established to probe short T2 tissue components, including magnetization transfer (MT) and ultra-short echo time (UTE) imaging. While promising, current clinical issue is limited by challenging interpretation of images.

MRI with ultra-short echo times (UTE) offers a dramatically improved the dynamic range of short T2 species (37). Typical UTE acquisitions are sensitive to species with a T2 as short as 200μs compared to the greater 1ms for conventional imaging. However, in the presence of long T2 signals, the short-T2 tissues are often obscured. Some form of long T2 suppression is necessary to selectively depict the short T2 components and improve the conspicuity of short T2 species. Current techniques for Short T2 separation include: 1) long T2 suppression through

magnetization preparation (44)(86)(87), 2) subtraction of a later echo from the initial echo(83)(40) or 3) fitting a T2* decay curve with a multicomponent model (88).

In idealistic situations, magnetization preparation techniques are preferred techniques. Current approaches utilize on-resonance {Larson} or off-resonance low-bandwidth irradiation[10], or inversion recovery to suppress long T2 signal and enhance short species contrast[7] . Unfortunately, these techniques are not robust or time consuming in practice. For example, methods based on low-bandwidth irradiation are sensitive to B0 variations and complicated by the presence of MT effects. On the other hand, inversion recovery can also be used to selectively null long-T2 components with a particular T1. Multiple inversion pulses maybe required to both null water signal and multiple resonance peaks fat signal(90). However, these methods are time consuming and may be problematic when imaging short T2 tissues because the broad spectral width of these species may overlap with that of fat and long T2 tissues. As a result, preparation pulses may inadvertently saturate the signal from short T2 tissues, either directly or as a result of magnetization transfer. Therefore, new methods are needed to overcome some of the aforementioned challenges and provide images with high contrast of short T2 tissues.

Multicomponent modeling of the T2* decay curve signal provides potentially more robust method of imaging short T2 species(61) (64). In this spectroscopic method, multiple echoes are collected and fit to bi-exponential decay curve. While more robust to B0 and fat than simple subtraction techniques, short echo spacing is required and thus a range of echo times are interleaved over multiple acquisitions. A typical effort requires an hour to map out limited coverage in ex-vivo tissue.

Here we report a new, highly efficient, B0 robust 3D least squares based UTE imaging method which allows for visualization of short T2 species. Though the method is not quantitative, substantial characterization of short T2 tissue is possible with a minimal increase in imaging time. The application of the method is demonstrated in depicting short T2 tissues in difficult MR environment such as the ankle and chest. Beyond characterizing short T2 tissue, we also demonstrate how the method could be used to segment bone, fat, and water for PET attenuation correction in multimodality PET/MRI systems.

3.2 Theory

The signal from a voxel containing water and fat from a spoiled gradient echo sequence is can be modeled as the following(14):

$$s(t) = \left(\rho_W + \rho_F C_F(t)\right) e^{-t/T2^*} e^{i\varphi t} \quad \text{Equation 1}$$

where ρ_W represents the water species, ρ_F represents lipid signal with a multiple peaks chemical shift $C_F(t)$ model, φ is the local magnetic resonance offset (Hz). Though T2* can vary between voxels, this model forces a single T2* value for voxels with a mix of water and fat(65). A variety of methods (e.g. IDEAL(22)) solve for fat and water even in the presence of substantial B0 heterogeneity.

Efforts at multicomponent mapping of water compartments with differing relaxation times acquire more samples (echoes) along the decay curve and thus can fit more free parameters. Acquisitions tailored to decomposing multiple components can use a more complex signal model that adds a short T2 species with varying T2* relaxation rate. These additional free parameters can be incorporated into Eq 1.:

$$s(t) = \left(\left(\rho_W + \rho_F C_F(t) \right) e^{-t/T2^*} + \rho_{T2} e^{-t/T2^*_{short}} \right) e^{i\varphi t} \quad \text{Equation 2}$$

where ρ_{T2} represents short T2 water species with a separate T2*: $T2^*_{short}$. With a $T2_{short}$ on the order of 500μs, multiple acquisitions are required with echoes times less than a 1ms precluding the use of single train of echoes to sufficiently sample signal decay. However, if only sensitivity to a single $T2_{short}$ species or group of short T2 species with relaxation rates generally known to be less than an upper limit, the signal can instead be expressed without the free parameter $T2^*_{short}$:

$$s(t) = \begin{cases} \left(\left(\rho_W + \rho_F C_F(t) \right) e^{-t/T2^*} + \rho_{T2} \right) e^{i\varphi t} & TE_0 \\ \left(\rho_W + \rho_F C_F(t) \right) e^{-t/T2^*} e^{i\varphi t} & otherwise \end{cases}$$

Equation 3

Where TE_0 is an echo acquired at an ultrashort echo time and all other echo times are assumed to be standard echo times. This model assumes minimal contributions of short T2 signal in the later echo time and further assumes negligible decay of the short T2 species before the first echo. By setting the first echo time to be at or less than the desired T2* of the short relaxation time of interest, we next study how valid this assumption is.

3.3 Materials and Methods

3.3.1 Digital phantom simulation

The performance of the UTE-IDEAL reconstruction algorithm was initially evaluated in digital phantom created in MATLAB (Natick, MA) with synthetic chemical shift encoded data for a 3T system with three variable components: water, fat and a single short-T2 signals. Five

echoes were used for the digital phantom creation with the initial echo of TE1=80us and echo spacing of ΔTE = 2ms. Synthetic fat data was encoded with a commonly used model with six off-resonance frequencies.

We simulated the signal of short T2 image of the UTE-IDEAL decomposition as the T2* of short-T2 components changes from very short to long relaxation time. In this simulation, the initial echo time and echo spacing was fixed at 80us and 2ms respectively and with T2* {0.1, 0.5, 1 2 3 10}ms. We also studied the changes in short-T2 signal with the changes in echo spacing. Here, initial echo time, T2* of short T2 phantom fixed at 80us and 0.5ms respectively and echo spacing changed from 1ms to 3ms with a 0.4ms increment.

3.3.2 Acquisition Sequence

A 3D UTE imaging was utilized for all experiments. The 3D UTE pulse sequence, shown in Figure 3.1, applies a short selective RF pulse (300 us). Given the 3D slab excitation, a minimal refocusing gradient was needed and thus the first TE was only 80 us. This is also the minimum time required for our unmodified hardware to switch from RF transmission to reception. This selective RF pulse is applied axially to limit the superior/inferior (S/I) excitation FOV and thus reduces artifacts due to aliasing. Sequences utilize RF and gradient spoiling (SPGR)(70).

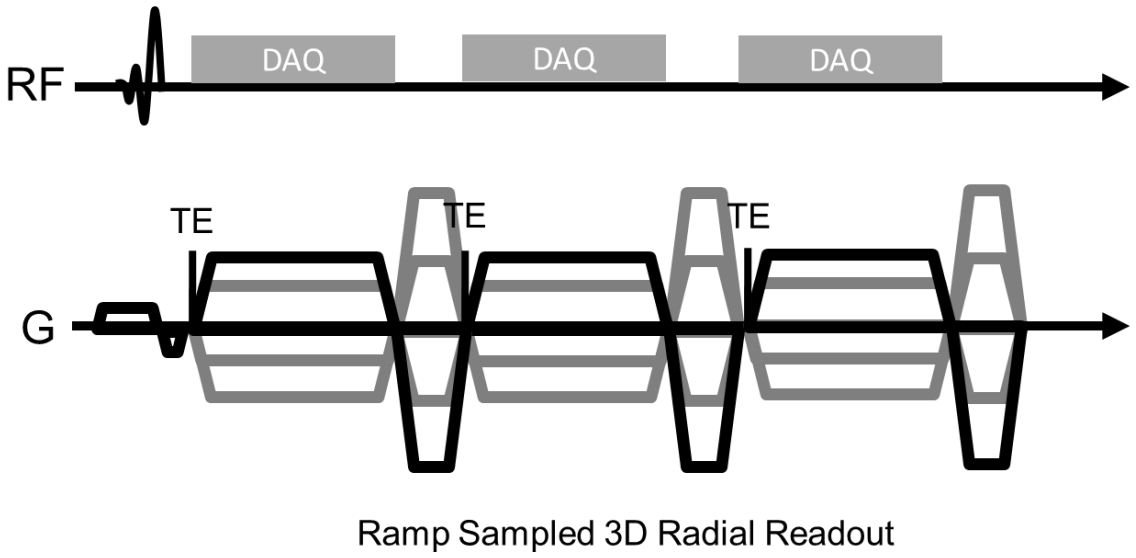

Figure 3.1 Pulse sequence diagram for multi-echo 3D UTE consisting of short RF excitation and flyback radial readout gradients.

3.3.3 Scanner Implementation

The proposed method was applied to image the Achilles tendon, meniscus and chest of healthy volunteers. Images of human volunteers were obtained on 3T scanner (Discovery MR750 GE Healthcare, Waukesha, WI) with a maximum gradient performance of 50 mT/m and 200 mT/m/ms. A standard 8-channel phased-array knee coil was used to image the knee and a standard 8-channel phased-array foot/ankle coil was used to image the ankle at 3T. Chest images were acquired using an 8-channel body coil. Five echo images were acquired for each scan with the center of k-space sampled at TE = 80 μs, 2.00 ms, 3.92 ms, 5.84 ms, 7.76 ms. Common imaging parameters for the knee and ankle included: FOV = 16 cm, bandwidth (BW) = ±125 kHz, flip angle =7°, actual matrix size = 320 x 320 x 320 and pulse repetition time =10.6 msec. 60000 half projections were acquired for each echo image resulting in a total scan time of 10.41 minutes. Chest images were acquired utilizing: 5 echoes (TE1=100μs, ΔTE=1ms), TR=10ms,

α=10°, 2.5mm isotropic image resolution, 30,000 projections. Respiratory gating was used during chest imaging (with 50% efficiency) yielding a scan time of ~10min.

Prior to imaging, informed consent was obtained from the volunteers. Product automated shim routines were used for all imaging.

3.3.4 Reconstruction process

Individual echo images were reconstructed and then processed by the modified IDEAL algorithm with the signal modeled in Equation 3. The implementation of IDEAL reconstruction can be summarized in the following three step process:

a) Perform robust image space IDEAL algorithm with T2* estimation and multi-peak fat spectral model on the reconstructed echo images to generate a B0 inhomogeneity map ψ(r) and R*2 (r) map.
b) Use the B0 inhomogeneity map and the R2* (r) map to process the complex echo images to remove confounding phase errors from B0 and signal decay due to R2*.
c) Decompose water, fat and short-T2 signal using a least-square approach and the actual readout time.

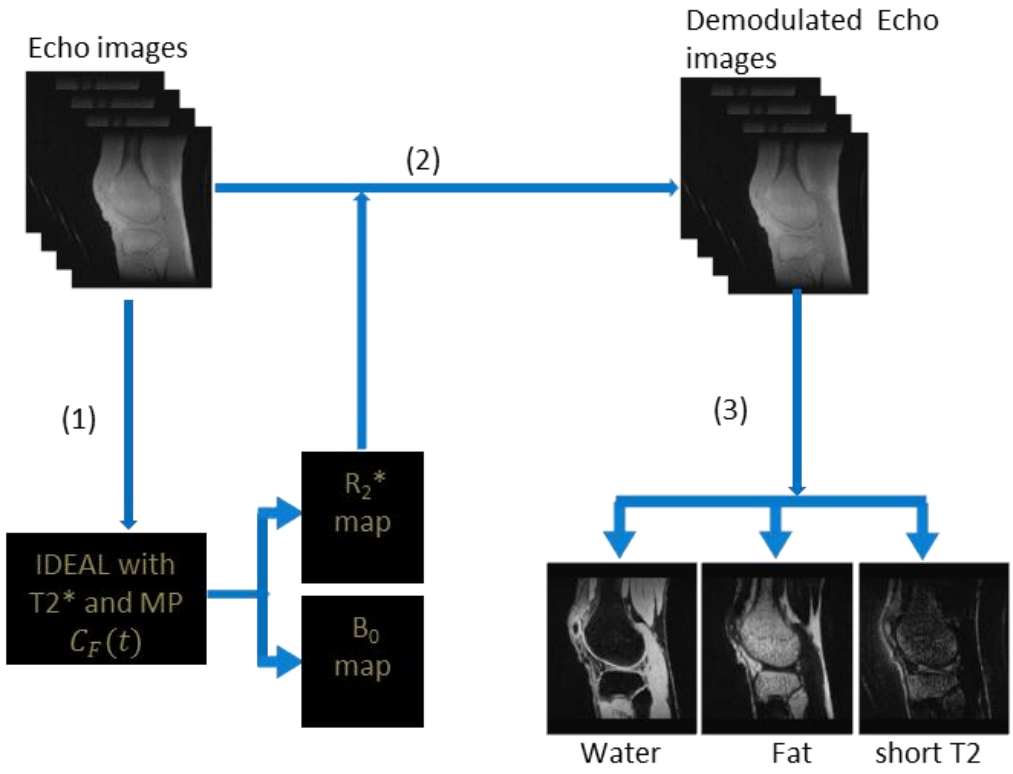

Figure 3.2 Schematic diagram of IDEAL-UTE decomposition method. IDEAL reconstruction applied on acquired echo images to generate B0 and R2* maps. Then maps used to obtain demodulated echo images. Finally, decomposed water, fat and short-T2 images obtained using least-square approach.

3.4 Results and Discussion

3.4.1 Simulation

The generated digital phantom simulations with fat, water short T2, and field map components is shown in figure 3. T2* of the short T2 species was set to 500μs and an initial echo time of 80μs was used with 1.92ms time interval between echoes. As seen in the images of figure 3, signal from the short T2 species is visible in the first echo image only and decays to zero before

the acquisition time of later echoes. True field map used for phantom creation is also shown in figure 3.

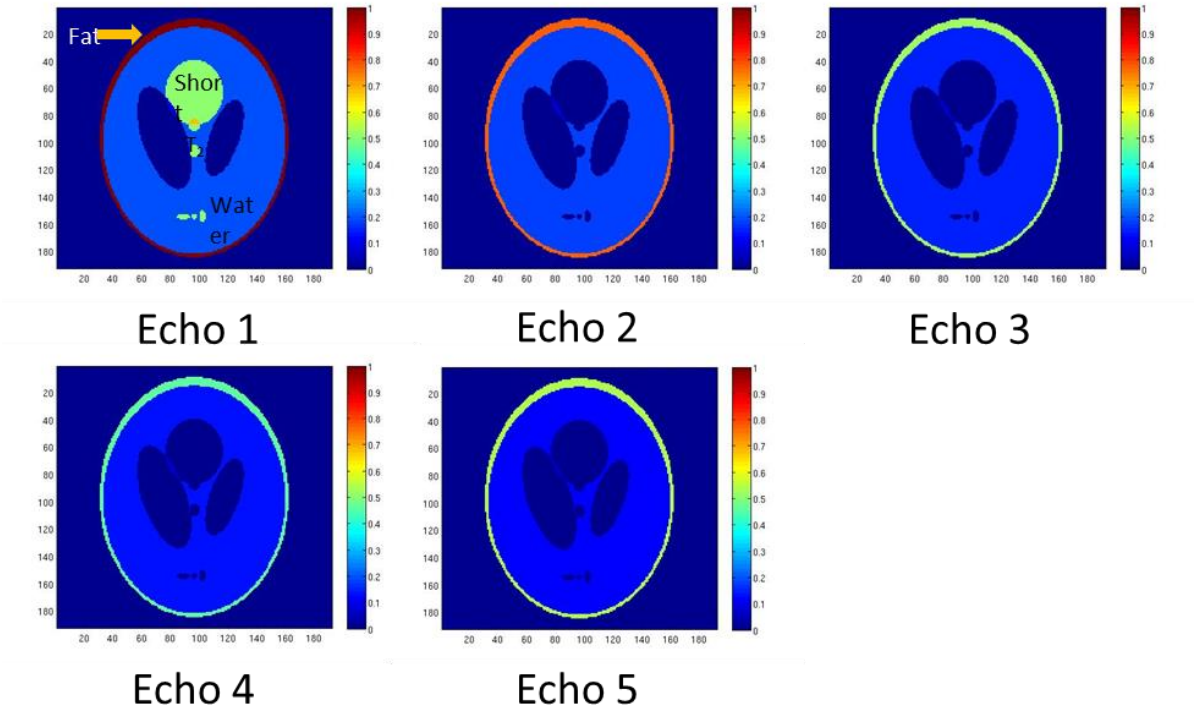

Figure 3.3 Digital phantom created with fat, water and short T2 components and used for simulation. T2* of the short T2 components set to 500**μs** and initial echo set to 80**μs** with 1.9ms spacing between echoes. In the five simulated echoes, short-T2 signal appears only in the first echo. Field map used for phantom creation is also shown.

Figure 4 shows water and short T_2 decomposition images of the digital phantom simulated with different relaxation times of the phantom's short T_2 species to illustrate the behavior of the IDEAL-UTE decomposition algorithm as the T_2 of the short components gets closer to that of water. With T2s longer than the second echo time, short T_2 signal components contaminate the water image and decrease in the short T_2 image. This is demonstrated in the 2ms and 3ms images of Figure 4. When the short T_2 species signal is long enough to appear in most of the echoes as

in the 10 ms case, all signal is assigned to the water image as expected and the algorithm behaves as the conventional IDEAL reconstruction. Figure 5 plots short T_2 signal in the decomposed short-T_2 image and water image as T_2^* varies from 80μs to 10ms with fixed echo times. Short-T_2 components were assigned completely to the short-T_2 image for T_2s shorter than the first echo time. Signals that persisted into the second echo and yet not long enough to exist in all echoes was distributed between the water and short_T_2 images. However, when the short-T_2 signal exists in all acquired echoes, the decomposition process works very well in assigning the signal to the moderate to long relaxation water image and goes to zero in the short-T_2 images as expected. We also simulated the signal of short T_2 species for different echo spacing times from the initial echo time and T_2^* value held fixed at 80μs and 500μs respectivly. Figure 6 shows that the calculated short-T_2 signal is independent of echo spacing for these very short T2 relaxation species. The results here complies in general with that calculated by Reeder et al. for conventional IDEAL (49).

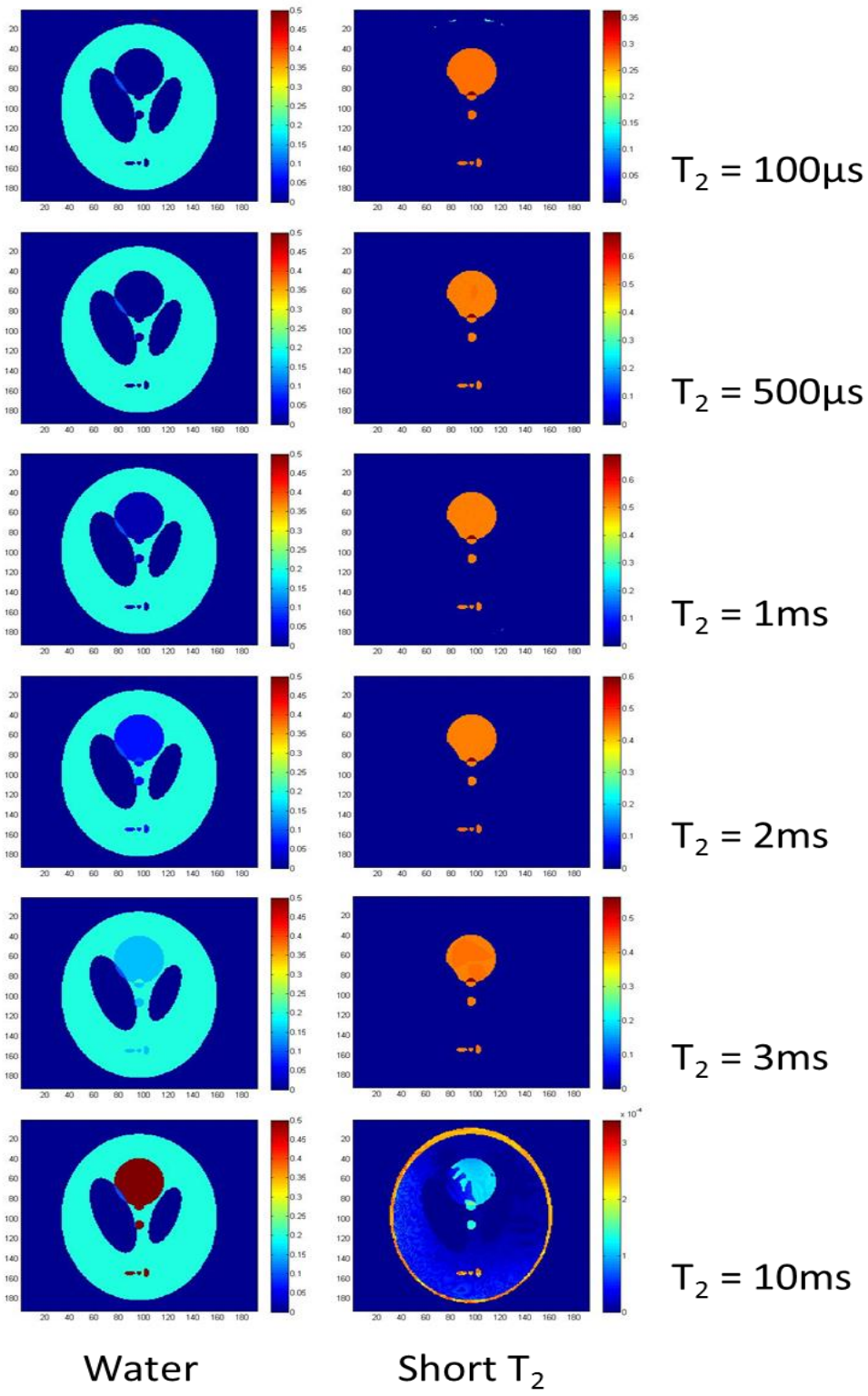

Figure 3.4 Simulation images of water and short T2 decomposition with different values of T2* of short T2 components.

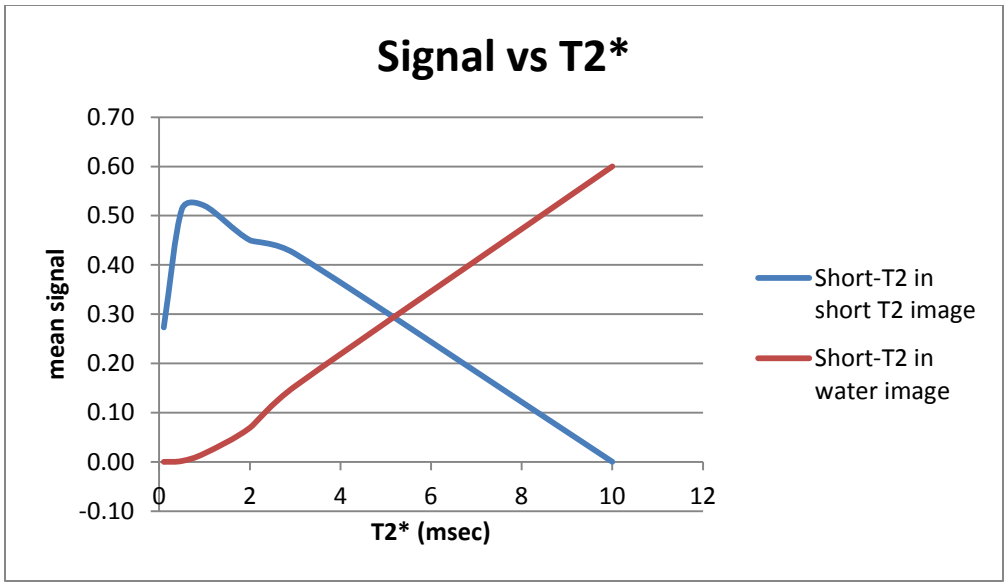

Figure 3.5 Signal of short-T2 species in the calculated short T2 and water images as function of short-T2 relaxation time.

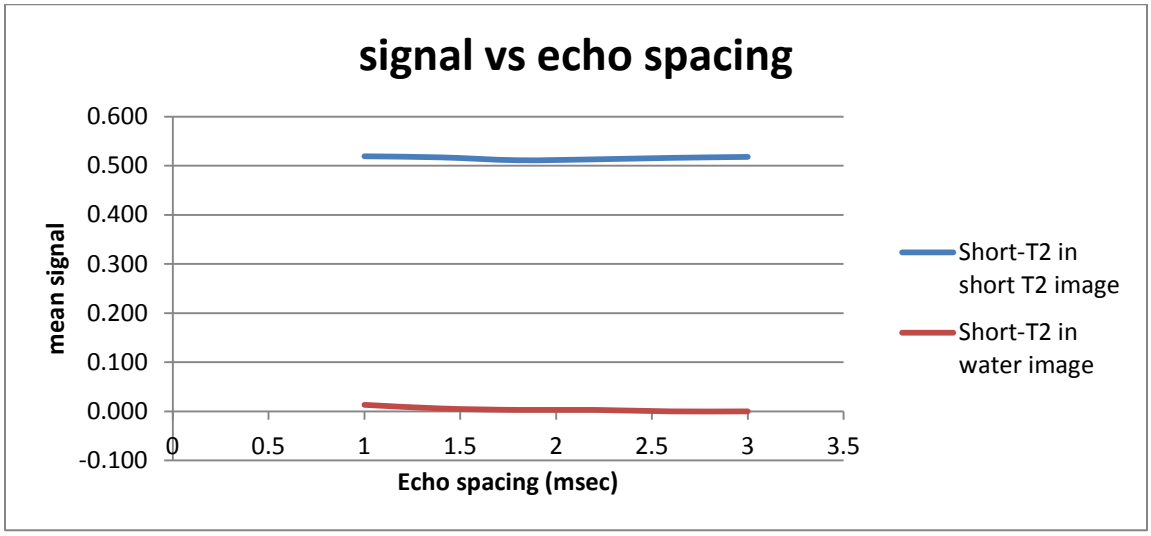

Figure 3.6 Signal of short-T2 species in the calculated short T2 and water images as function of echo spacing for very short T2* species less than 1 ms..

Examples of the calculated fat, water and short T_2 images are shown in figs. 3-4. Conventional UTE two echo subtraction images are shown also for comparison. Figure 3 shows the

comparison between the UTE subtraction method for long T_2 suppression and UTE_IDEAL method for a human knee in the sagittal plane. Uniform fat–water separation was achieved and long T2 components are completely suppressed in the short T2 image provided by IDEAL-UTE. Compared to the simple, conventional difference image on the top row, the short T2 image from IDEAL-UTE demonstrates a significant contrast increase between the menisci and surrounding cartilage.

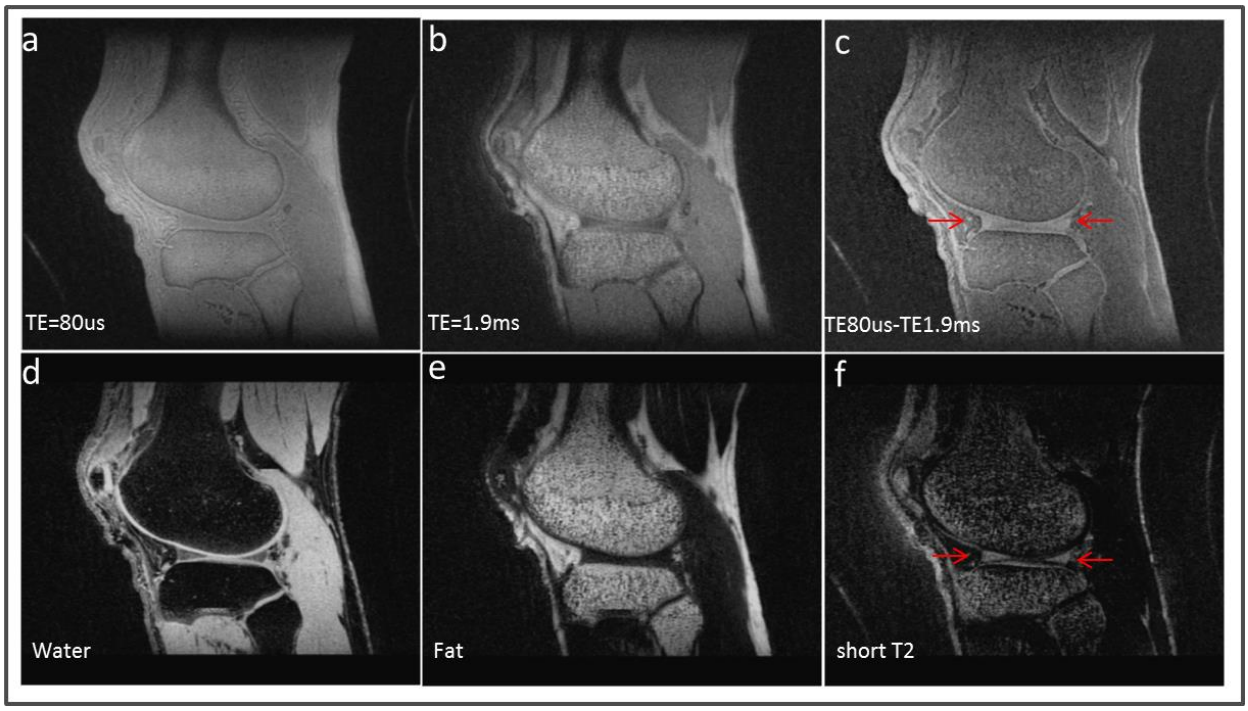

Figure 3.7 sagittal images of UTE short echo (a), second echo (b), subtraction (c), IDEAL-UTE water image (d), IDEAL-UTE fat image (e) and IDEAL short-T2 image (f). Meniscus (arrows) is highlighted in short-T2 image.

In Figure 4, we compared performance of the previously described Inverted Double Half RF pulse (IDHRF) [9] used to null excitation of fat and longer T2 species with the IDEAL-UTE in the Achilles tendon. While IDHRF showed the desired suppression near the Achilles tendon, it

fails in other areas (red arrows) due to errors in field inhomogeneity. The short T2 image of the IDEAL-UTE shows enhanced depiction of the Achilles tendon, other tendons not visualized in the IDHRF image, and uniform fat and water suppression over the entire joint. The fractions of short and long T2 components can also be obtained from water and short T2 images.

The 3D UTE SPGR sequence with multi-echo acquisition and IDEAL reconstruction provides high contrast imaging of short T2 species despite B0 inhomogeneity while also robustly suppressing fat.

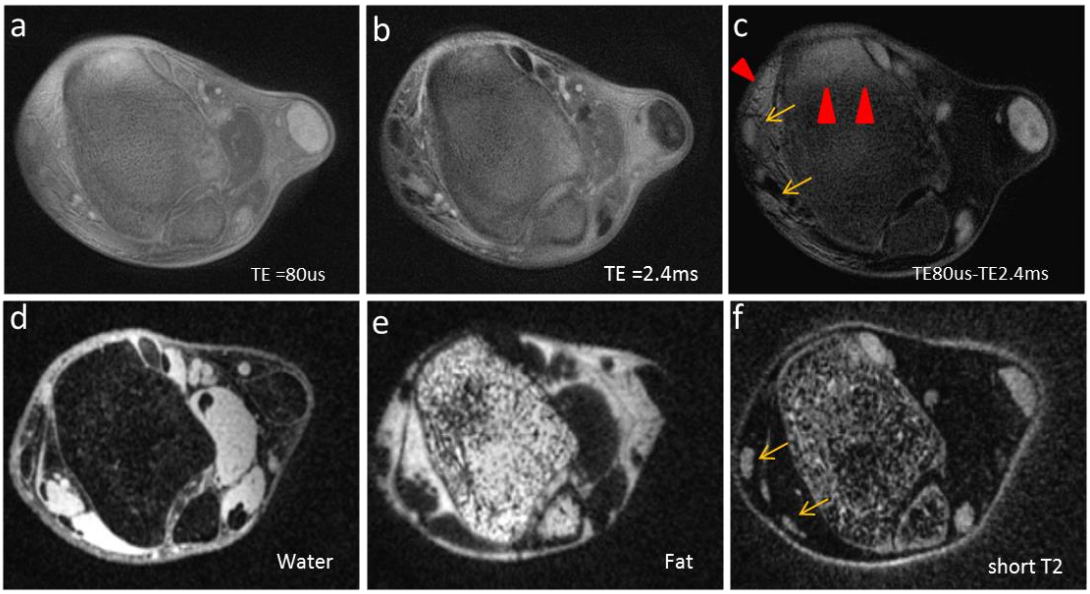

Figure 3.8 Axial images of IDHRF UTE, short TE (a), second echo (b), subtraction (c) and IDEAL UTE water image (d), IDEAL fat image (e) and IDEAL short-T2 image (f). IDHRF UTE failed to completely suppress long-T2 components (red arrows) due to B0 inhomogeneity while the IDEAL UTE decomposition works robustly throughout the ankle.

A single axial slice from a whole-chest image volume is shown in Figure 9. Left (a) and center (b) images show the conventional water and fat components respectively, exclusively from soft

tissue. The short-T2 component image (c), however, clearly demonstrates signal levels from short T2* components including cortical bone along the scapula, ribs, and in both lungs regardless of the presence of marrow. Note this method images bone due to sensitivity to its short T2 components rather the presence of marrow, which is only present in long bones in the body.

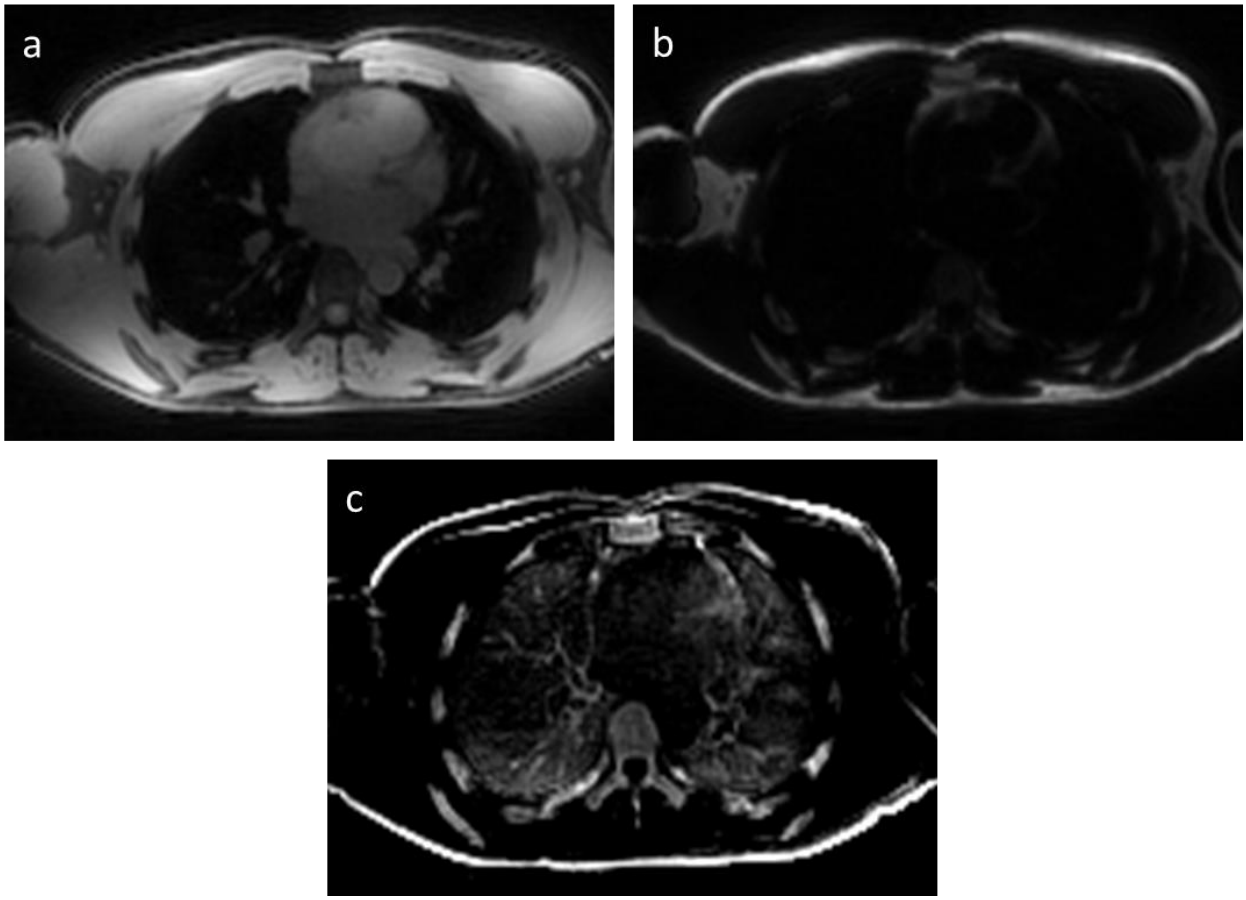

Figure 3.9 Axial chest images show water (a), fat (b), and short T2 (c) components. The short T2 image (c) allows a distinct view of bones (ribs, vertebrate, sternum, and scapula).

3.5 Conclusion

In conclusion, we have presented a new short T2 tissues signal contrast enhancement method for UTE applications that is robust to variations in the $B0$ and B1 fields by using chemical shift-based water-fat separation method to create short-T2 contrast. The proposed method combines the 3D UTE data acquisition sequence with the IDEAL reconstruction technique to provide high contrast imaging of the short T2 tissues with robust fat water separation. Applications of this method in phantom and human knee and ankle were shown. Compared to existing long T2 separation methods, the UTE-IDEAL method offers improved fat and water decomposition and improved short T2 components visualization in tendon and meniscus in joints as well as in areas that have susceptibility changes such as chest.

Chapter 4:

3D Radial Under-sampling Artifacts

In the previous two chapters, we demonstrated that 3D radial imaging methods, such as VIPR-ATR and IDEAL-UTE, have proven to be powerful for the knee joint assessment by consistently providing 0.3 mm isotropic resolution which may be reformatted along any orientation only eight minute. Undersampling in the azimuthal and elevation dimensions of the k-space sphere can actually increase resolution with no increase in scan time when the imaging environment has sparse, high contrast to noise signal.. However, the effects of 3D undersampling in instances when the data are not sparse, such as in morphological musculoskeletal imaging, can rapidly degrade the apparent image SNR(66). Phase array coils can be quite valuable in improving 3D radial imaging due to PILS effect(67).

This chapter quantitatively and qualitatively demonstrates the benefits of increased coil sensitivity in the azimuthal dimension for given high isotropic resolution and fixed scan time to assess cartilage volume measurements. In-vitro and in-vivo results, demonstrate higher image quality than previously attainable at high resolution with the conventional phase array coil.

4.1 Partially Parallel Imaging with Local Sensitivities (PILS)

The impulse response of the 3D radial trajectory consists of a properly imaged localized spherical FOV with weaker undersampling artifacts extending beyond this region. The number of radial lines, Nr, necessary to meet the Nyquist criteria is

$$N_r = \pi N_{res}^2$$

Where N_{res} is the resolution. The number of resolution points needed to depict the region decreases with the size of the sensitivity region as the coil gets smaller as illustrated in figure 4.1. Thus, the number of radial lines which must be sampled decreases as the square of this reduction. Griswold has termed this the Partially Parallel Imaging with Localized Sensitivities (PILS) effect, for its similarity to his Cartesian parallel imaging method where the number of phase encodes is determined by the coil sensitivity dimension instead of the imaging FOV (94).

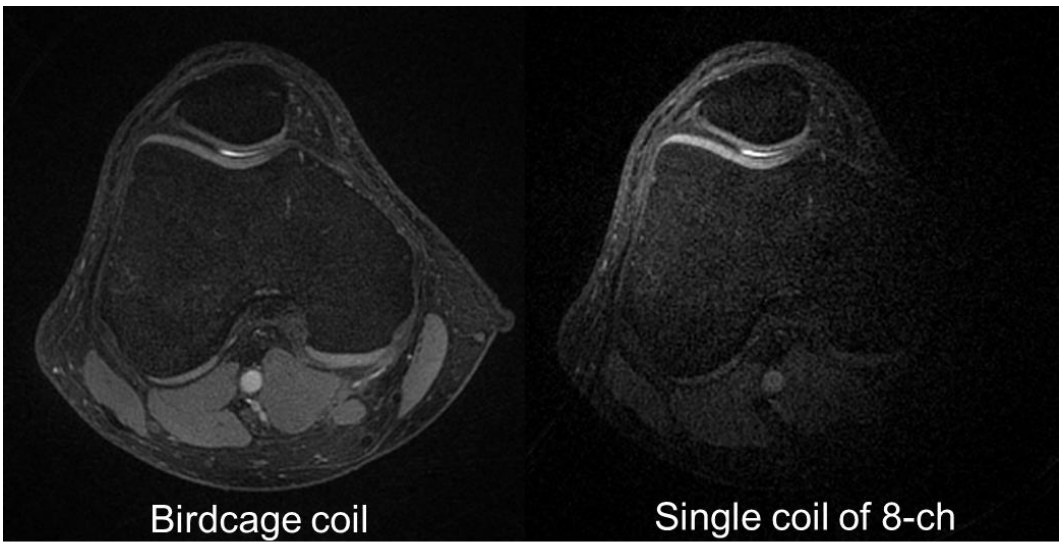

Figure 4.1 The number of resolution points needed to depict a coil sensitivity region covering the entire knee joint is far more than the number needed to depict the coil sensitivity region on the right, which is one of eight coil elements.

SNR drops by the square root of the acceleration factor for properly sampled MR scans. When radial scans are accelerated by reducing the number of sampled radial lines, SNR drops more rapidly due both to shortened acquisition time and undersampling artifacts. If an improved coil with more receivers both improves SNR and reduces the size of the sensitivity region, radial trajectories can be accelerated with essentially no loss in SNR. In accelerated Cartesian parallel MRI, more elaborate reconstruction algorithms are necessary, even for methods as fundamental as PILS. As the impulse response of the radial trajectory is properly located, the radial PILS effect can be exploited with no change in the reconstruction algorithm.

4.2 Improved Performance with 16 Channel Coil: Quantification of Unedersampling Artifacts with 8 and 16 Channel Knee Coils

4.2.1 Introduction

Large phased arrays coils are arranged in multiple rows normally to enable parallel imaging acceleration in more than one dimension. As image resolution is paramount in joint imaging, phased array coils are utilized for a more conventional purpose, improved SNR. However, radial imaging has been shown to improve dramatically with larger phased arrays coils due to the PILS effect1. We hypothesize that the asymmetry of a single row coil allows the PILS effect to only be partially exploited in 3D radial imaging. We utilize a means to estimate aliasing's contribution to noise-like variance and demonstrate the significant benefits of reducing aliasing with a 16-channel, 3 row knee coil relative to- a conventional 8-channel single row knee coil.

4.2.2 Methods

For a single channel coil, the number of acquired radial lines necessary to fully sample a spherical volume increases as the image matrix size, Nr, squared. Specifically $N_{TR} = \pi N_r^2$ (Eq. 1) where NTR = number of radial lines. However, the PILS effect states that individual coils in phased array systems are sensitive to a smaller subvolume of the entire image1. Thus Nr is effectively reduced, which in turn decreases the actual number of radial lines that need to be acquired. A typical 8-channel knee coil is arranged entirely in a single row about the physical z-axis. While the effective image matrix for each coil is reduced in the transverse plane, there is no differential S/I sensitivity and thus no reduction of the image matrix in that dimension. we compared an 8-channel single row knee coil (GE/Invivo Precision) to a 16-channel knee coil (GE NeoCoil, Pewaukee,WI) split in 3 rows of 5,6 and 5 elements to determine if the increased sensitivity in the S/I direction improved performance over a single row coil design. A 0.33 mm isotropic, 8 minute scan was utilized to challenge imaging performance with a theoretical undersampling factor of 5 (Eq. 1) on a GE 750 3T scanner. Scans were also repeated with increasing acceleration (5,10,20) to increase undersampling artifact while signal averaging was increased to keep the same level of stochastic noise. Any increase in the variance over ROIs of comparisons of the same region is thus due to undersampling.

Measuring performance in the presence of under sampling is object-dependent and thus difficult. To separate the effects of stochastic noise and noise-like artifacts from under sampling, scans were repeated with different acceleration factors (5,10,20) to vary under sampling artifact while signal averaging was utilized to keep the same level of stochastic noise. Any difference in the variance of ROI comparisons of the same region is then due to under sampling.

Studies were conducted on a GE 750 3T scanner (GE Healthcare, Milwaukee, WI) over a 15cm FOV using a 16 channel (GE NeoCoil, Pewaukee,WI) and 8 channel phased-array extremity (Invivo, Orlando, FL) coils and the VIPR-ATR sequence. Efficient radial encoding with dual-half echo acquisition over 416^3 image matrix allows for 0.33 mm resolution, with no increase in TR and thus no increase in sensitivity to off-resonance at 3.0T. High resolution images from both the 16 and 8 array coils are provided for comparison in image quality.

4.2.3 Results

Table 4.1 shows a comparison of variance due to tissue and surface coil variation and undersampling over an ROI as undersampling is increased while stochastic noise is held constant. The study shows that the 16-channel coil has some headroom to accelerate through undersampling while artifacts due to undersampling rapidly escalate with the 8-channel coil.

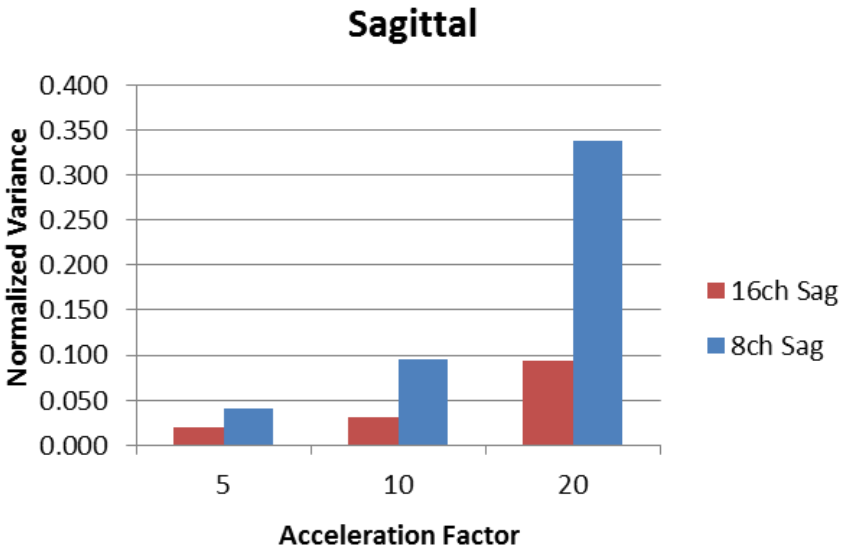

Table 4.1 The magnitude of artifact due to aliased, undersampling artifacts and the rate at which it grows with acceleration factor is lower for the 16 channel coil with S/I sensitivity.

While comparing exactly the same anatomy is difficult due to differences in the knee flexion created by each coil, the 16 channel coil significantly reduces noise-like artifacts due to undersampling that improve depiction of the meniscus, bone-cartilage interfaces, and muscle, as shown in Figure 4.2.

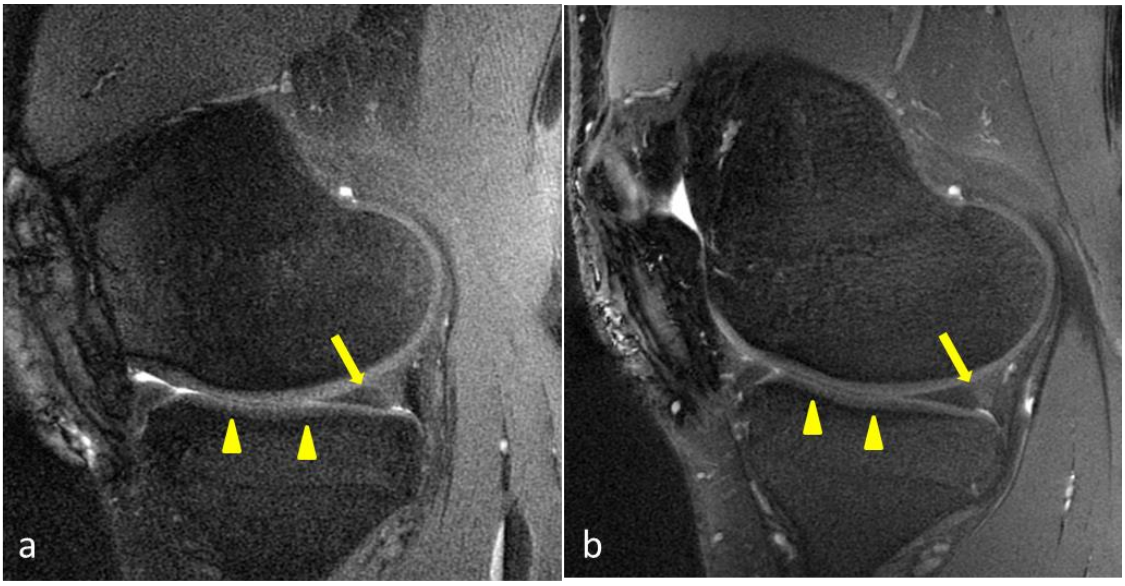

FIGURE 4.2 Improving performance using coils with S/I sensitivity. Note improved bone-cartilage interface (small arrows, meniscus (large arrow) and muscle depiction in (b) due to reduced noise-like aliasing energy.

In Figure 4.3, the 16 channel coil performs remarkably well at this challenging resolution in depicting the patella cartilage, removing mottling in bone, and is especially evident in the posterior vasculature. Performance improvement at challenging resolutions with 16 channel coils is much higher than one could expect when using a Cartesian sequence.

FIGURE 4.3 Improved performance demonstrated in the axial plane with 0.33mm isotropic resolution. Cartilage SNR is degraded in the 8-channel image due to under sampling compared to the16-channel image (arrowheads). Aliasing in the patella bone in (a) ,which could be confused with bone marrow edema, is also eliminated in (b)(large arrows).

Figure 4.4, shows comparision of image quality in the axial plane between 8-channel and 16-channel coil for three acceleration factors, 5, 10 and 20. Undersampling noise totally obscures petalla cartilage in the 8-channel coil image when undersampled by factor of 20. On the other hand, even with acceleration of 20, cartilage in the 16-cchannel exam is still visible compared to 8-channel.

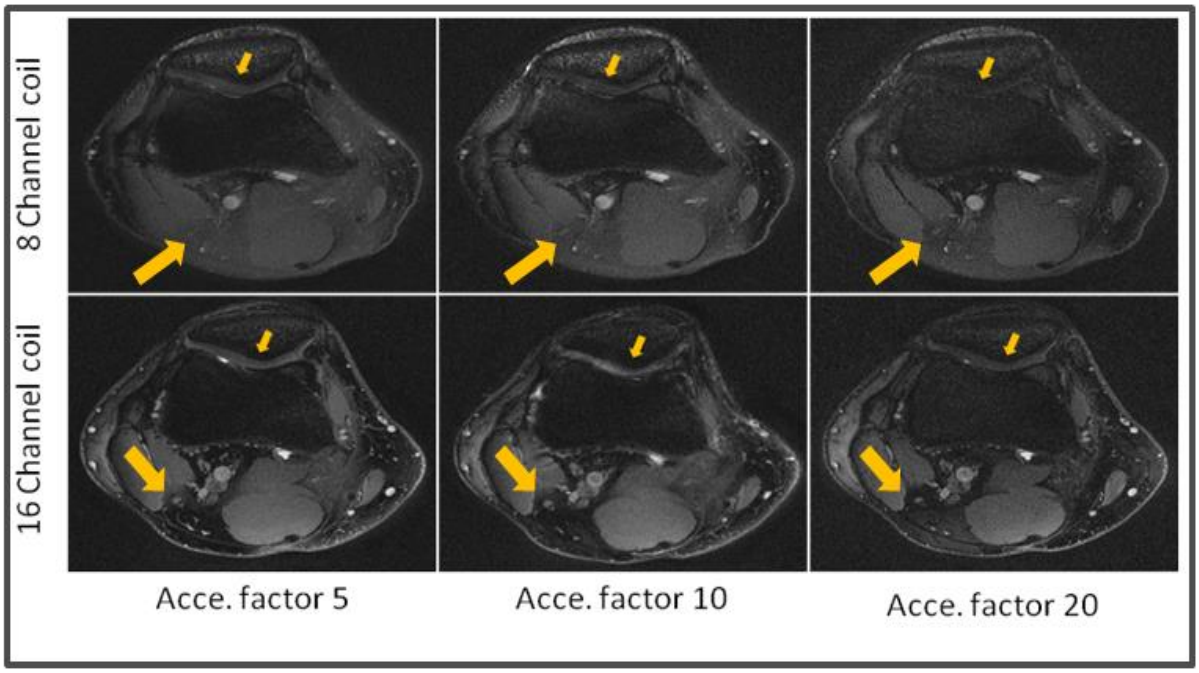

Figure 4.4 Visualizing undersampling, Even with acceleration of 20, patella cartilage is visible with 16 channels (bottom).Undersampling totally obscures patella cartilage with 8-CH (top).

4.2.4 Conclusion

Providing S/I sensitivity through the addition of coil elements in rows in the S/I dimension allows commercial coils to fully exploit the PILS effect in high performance 3D radial joint imaging.

Chapter 5:

Imaging of Joint Structure with Limited Free Water Using UTE

5.1 Introduction

The musculoskeletal system has an abundance of short T2 tissues including the calcified layer of cartilage and bone, tendon, the knee meniscus, cortical bone, and ligaments. These tissues have T2 relaxation times in the range of 0.4 ms to 2ms and the MR signal of these tissues significantly decays before conventional clinical imaging sequences complete signal acquisition. Traumatic changes to tendon, ligament and other short T2 tissues, like ruptures where liquid seen at the site, can be appreciated with conventional MR methods. However, the ability to visualize these tissues has important implications for offering insight into degenerative process, assessment of injury and pathogenesis of degenerative disease.

Ultra short TE (UTE) imaging with half pulse excitation and center out trajectories reduces the minimum echo time to ~200us dramatically improving visualization of short T2 species(95).

However, with half pulse excitation signal from short T2 components is often obscured by strong signal from fat and long T2 tissues. Fat saturation preparation pulses such as ChemSat pulse and double inversion recovery pulse can be used to suppress fat signal and enhance short T2 species contrast. These magnetization preparation methods are time consuming and worthy of further investigation. Inverted double half RF pulse (IDHRF) as described by Sonal J et al, selectively excites short T2 and improves out-of-slice cancelation results from eddy current errors (96). Sonal showed promising result with phantom study at low field strength (0.5T) for interventional application. In this work, we redesigned this pulse to provide fat suppression without using fat saturation preparation pulses. We investigated the use of this method at high field strength (3T) and demonstrate the capabilities of this pulse in musculoskeletal imaging of patella, tendon and ligament.

Alternatively, 3D UTE imaging have been performed using nonselective RF excitation with 3D radial FID sampling, yielding image data with isotropic spatial resolution (38)(39)(40). Like 2D UTE imaging, short T2 components are separated from longer components by either: 1) long T2 suppression through magnetization preparation, 2) subtraction of a later echo from the initial echo or 3) fitting a T2* decay curve with a multicomponent model. The latter two methods fail in regions of elevated B0 inhomogeneity. Here we report a new 3D IDEAL-based UTE imaging method which uses least squares fitting to explicitly calculate and compensate for B0 inhomogeneity while separating signal from short T2 (signal present only in first echo), long T2 species (signal present in all echoes), and fat.

5.2 Materials and Methods

5.2.1 Improved Selective Excitation of Short T2 Components in 3T Joint Imaging Using IDHRF

A 2D UTE sequence was implemented on a 3T Signa MR750 (GE Systems, Waukesha, WI) with the pulse sequence diagram shown in Figure 5.1. A pair of half sinc pulse with opposite polarity is played during each excitation followed by center-out radial data acquisition. All spins are tipped to the transverse plane by the first half RF pulse. Long T2 spins experience a negligible decay in the delay time and hence tipped back to the longitudinal axis by the second half RF pulse. However, the transverse magnetization of short T2 components destroyed in the time interval between pulses by short T2 decay and then excited again by the second half. The delay time between pulses was chosen so that fat spins be in phase by the end of excitation and hence suppressed too.

In this work, the separation time between the two half pulses is designed so that the lipid spins will be in phase by the end of each excitation, so the second half pulse will tip the lipid spins back to the longitudinal axis. For better short T2 contrast, a second image is acquired at later echo time and subtracted from first image. The time between the two echoes is also chosen so that lipid spins are in phase by end of the second echo for more fat suppression. For each pair of RF pulses, a precompensating negative gradient lobe was added before the slice-select gradient for better eddy current cancelation as suggested in (96).

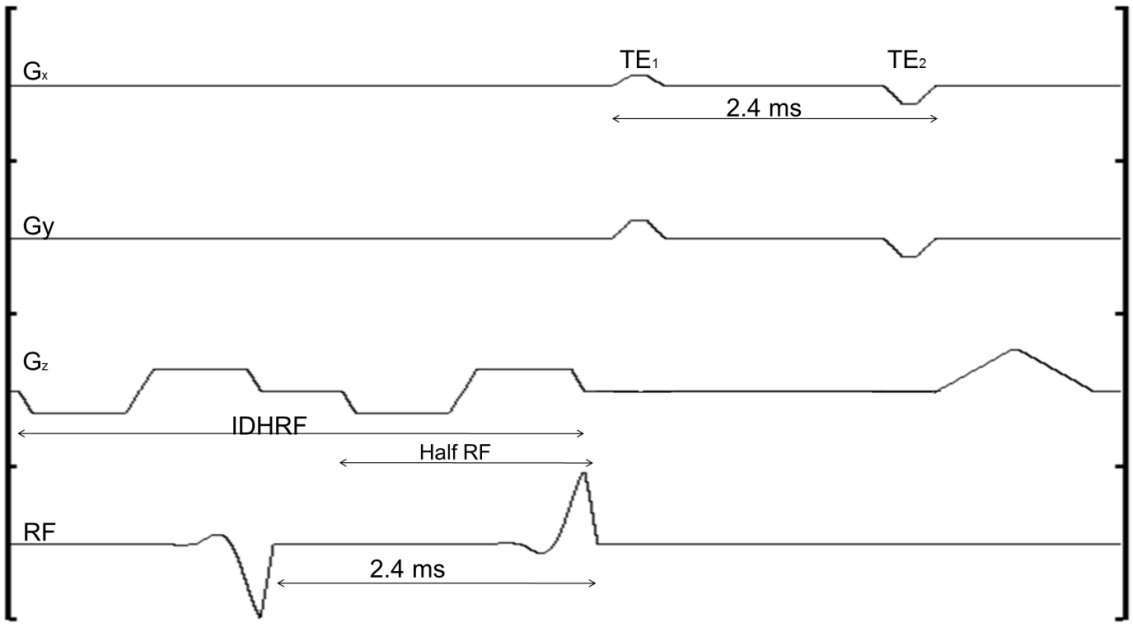

Figure 5.1 The inverted double half RF pulse sequence.

Experiments were performed on a phantom and a healthy volunteer to demonstrate the potential of this method at 3T. The phantom consists of four vials: one filled with vegetable oil (representing fat) and three filled with distilled water doped with different concentrations of Copper Sulfate (CuSo4) leading to transverse relaxation times of 100ms(water vial), 2ms and 0.5ms. Imaging parameters for the phantom study included: TE1 = 0.2ms,TE2=2.4ms, BW =+/- 125 kHz, TR = 30ms and 15 flip angle. Volunteer study parameters included: TE1 = 0.2ms, TE2 =2.6ms, TR =400ms (actual imaging time is 10ms), flip =22, BW = +/_125kHz and FOV = 15cm. scan time was 4min per slice.

5.2.2 Achilles Tendon Imaging in 3T with an inverted double half rf pulse excitation

A 2D UTE sequence was implemented on a 3T Signa MR750 (GE Systems, Waukesha, WI), with a 2D radial out and back data acquisition. Ramp sampling was used to achieve a minimum TE of 80 us. 2.4 ms prior to the conventional half pulse excitation, an inverted half pulse is

played to effectively create a null flip angle for fat and longer T2 components of water signal. Two excitations with inverted slice-select gradients are combined to form the final image.

Experiments were performed on a volunteer with chronic tendinopathy. Two four minute IDHRF scans were acquired with a resolution of 320x320 image matrix and 15cm FOV. The first IDHRF scan was performed with the shortest achievable echo time (80us). For a better fat suppression, a second IDHRF scan was acquired at a delayed echo and subtracted from the first image. The same two scans were repeated using the conventional half RF pulse for comparison. Study parameters included: TE1/TE2/TR 0.08ms/2.4ms/400ms. Scan time was 4min.

5.2.3 High Contrast 3D IDEAL Ultrashort TE (UTE) Imaging

A 3D UTE sequence was implemented on a 3T scanner (MR750, GE Healthcare, Waukesha, WI, USA) utilizing a short selective pulse to immediately followed by multi-echo 3D radial ramp sampling for data acquisition. IDEAL allows one to model various signal contributions and B0 inhomogeneity simultaneously. We developed the following signal equation for a three species signal model (short T2, all other water, and fat):

$$s(t) = \left(\rho_{T2} e^{-t/T2} + \rho_W + \rho_F C_F(t)\right) e^{-\varphi t} \quad \text{Equation 1}$$

where ρ_{T2} represents short T2 species with negligible signal after the first echo, ρ_W represents long T2 water, ρ_F is fat with multi-peak chemical shift $C_F(t)$, and φ is off-resonance and T2* decay. Images were acquired for the entire knee joint and Achilles tendon of a healthy volunteer in separate 10 minutes scan time utilizing: five echoes acquired starting at 80μs with 1.8ms echo spacing, resolution=0.5mm isotropic, 16cm3 FOV, BW=±125 kHz, flip=7°. Individual echo

images were reconstructed and then processed by the IDEAL algorithm with the signal modeled in Equation 1.

5.3 Results

5.3.1 Improved Selective Excitation of Short T2 Components in 3T Joint Imaging Using IDHRF

No eddy current correction was used in any acquisition. Figure 5.2 illustrates the short echo (0.2ms), late echo (2.4ms) and subtracted images for half pulse and IDHRF UTE sequences. Both sequences show signal from short T2 vials. In the short echo images, fat signal is reduced by 50% in the IDHRF image compared to half RF UTE. Subtracting short and long echo time images with half-pulse UTE results in reduced fat signal but the signal is substantially higher than with the IDHRF method with two echo subtraction.

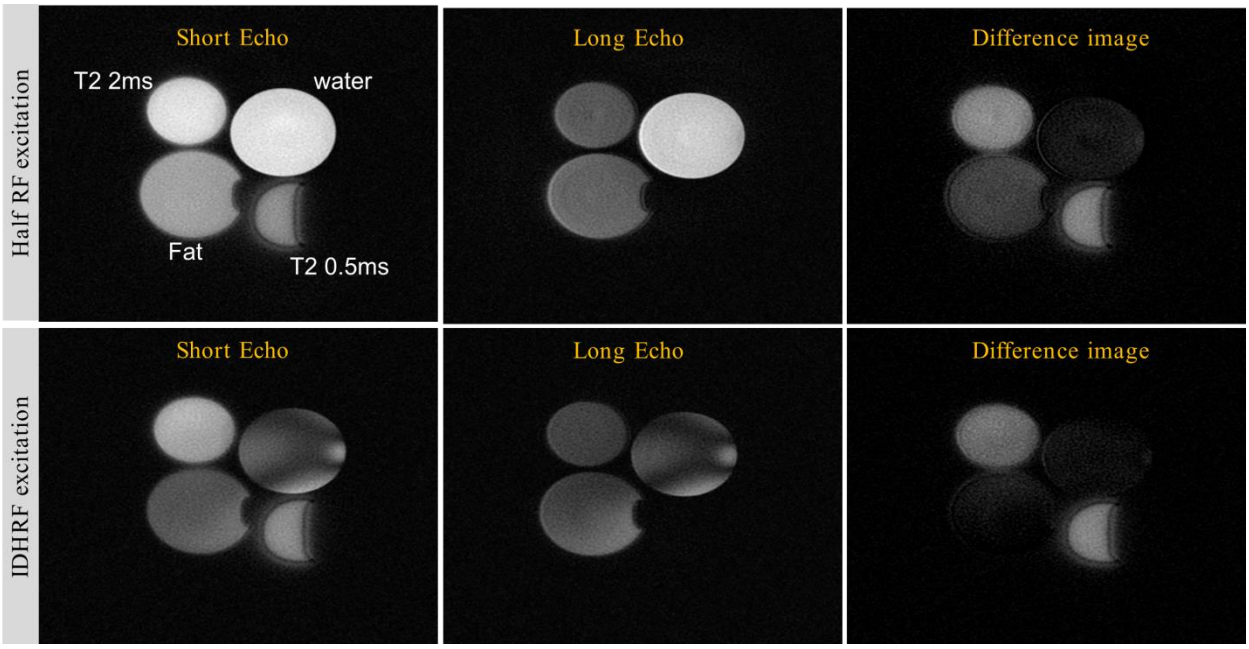

Figure 5.2 Short TE (0.2ms) and long TE (2.4ms) and difference images of half RF (Top) and IDHRF (bottom). IDHRF suppress water in short TE excitation and most of fat signal. Fat is highly suppressed in IDHRF difference image.

Difference images of later echo (2.4ms) subtracted from early echo (0.2ms) for IDHRF and half RF pulses are shown in Figure 5.3. The contrast of the origin of PCL (big arrow) and deep layer cartilage (small arrow) is improved in the IDHRF image compared to the half RF image as a result of increased fat suppression in bones. Suppression of fat in the fat pad behind the patella in the IDHRF image is also improved. Patellar tendon is highlighted in both images with better contrast in IDHRF image. In this work, only one slice was acquired per TR. In future work, up to 40 of interleaved slices per TR could be acquired.

Figure 5.3. Difference images of half RF (left) and IDHRF (right) pulse sequence are shown. The contrast of origin of PCL (thick arrow) and deep-layer cartilage (thin arrow) is improved in IDHRF image compared to half RF, as well as quadriceps tendon (large arrow head)and periosteum (small arrow head).

5.2.2 Achilles Tendon Imaging in 3T with an inverted double half rf pulse excitation

No eddy current correction was used to improve the half echo excitation in any acquisition. Figure 5.4 illustrates the short echo (0.08ms), late echo (2.4ms) and subtracted images for half pulse and IDHRF UTE sequences. Both sequences demonstrate signals from short T2 spins in tendon. High signal from the fat pad, muscles and bone are better suppressed in the early echo image of the IDHRF sequence compared to conventional Half RF pulse excitation. While the Achilles tendon signal is enhanced in both methods, the subtracted IDHRF image shows better overall attenuation of longer T2 species, better depiction of the edge of the tendon, and higher conspicuity of all tendons in the ankle against the background.

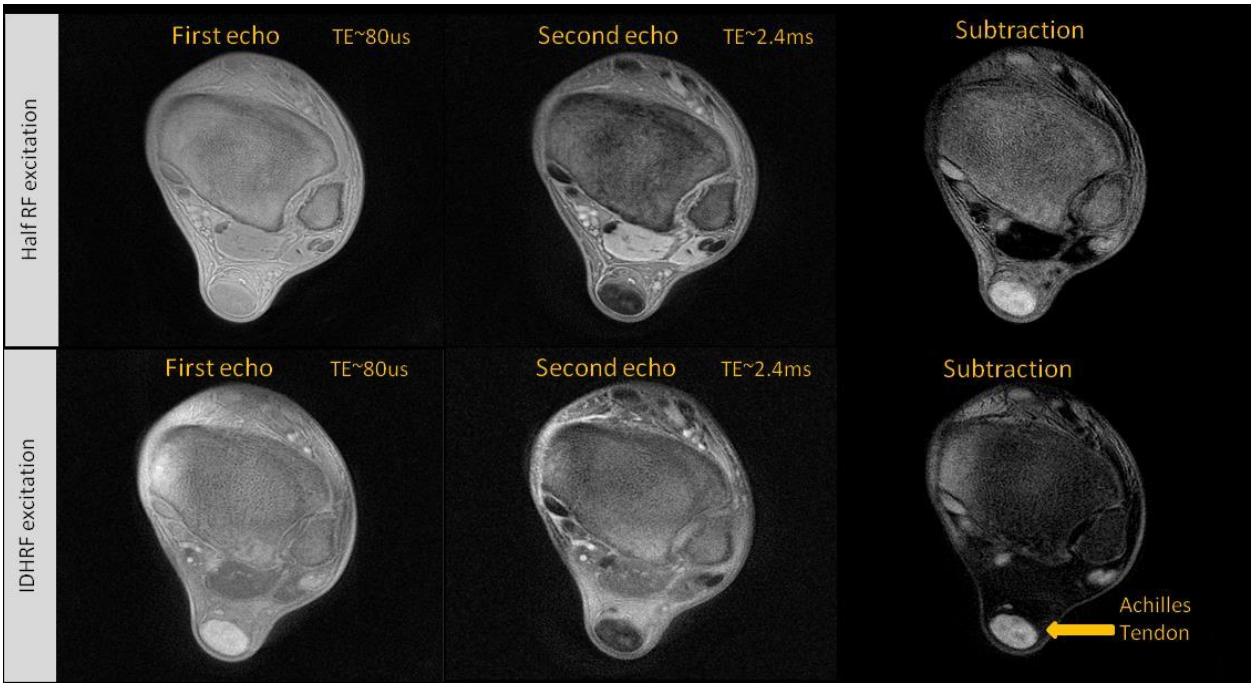

Figure 5.4 First, second and Difference images of half RF (top) and IDHRF (bottom) pulse sequence are shown. The contrast of the tendon is improved in IDHRF first and difference images compared to half RF due to better fat suppression.

5.3.3 High Contrast 3D IDEAL Ultrashort TE (UTE) Imaging

Figure 5.6 shows conventional UTE (top) and IDEAL-UTE (bottom) images for a human knee in the sagittal plane. Long T2 components are completely suppressed in the short T2 image provided by IDEAL-UTE. Compared to simple, conventional difference image on the top row, the short T2 image from IDEAL-UTE demonstrates a significant contrast increase from the menisci.

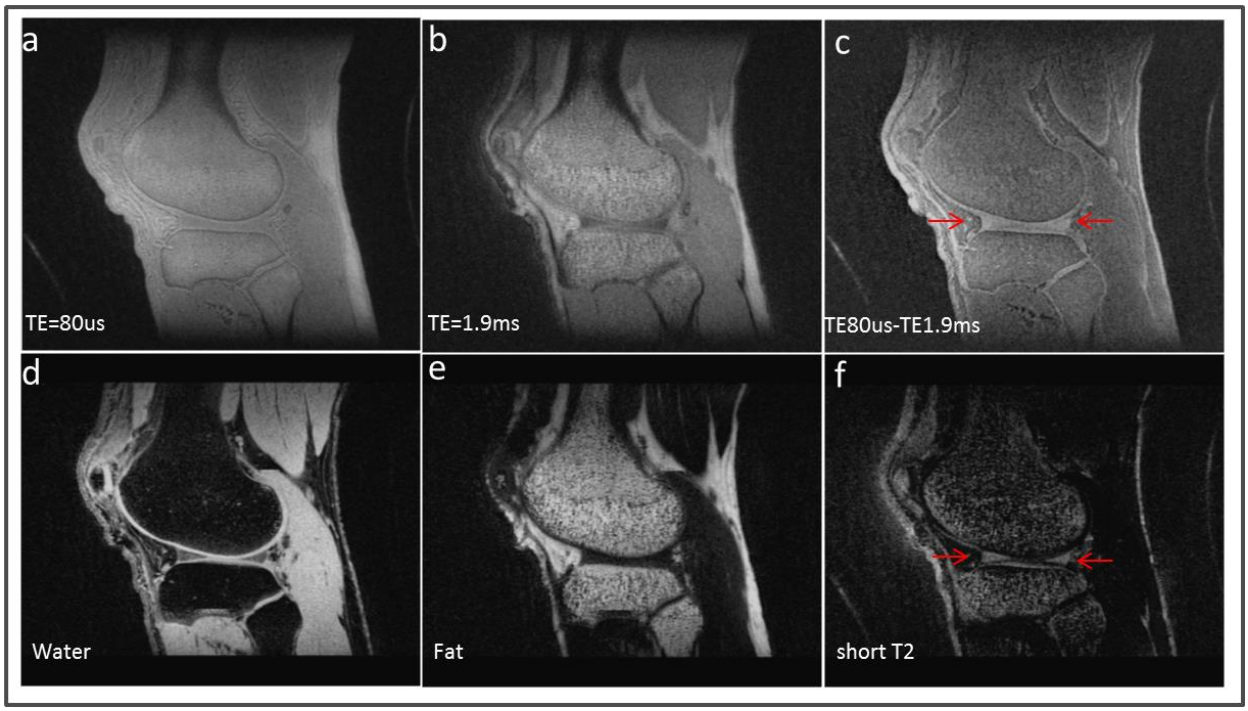

Figure 5.6 sagittal images of UTE short echo (a), second echo (b), subtructuion (c), IDEAL-UTE water image (d), IDEAL-UTE fat image (e) and IDEAL short-T2 image (f). Meniscus (arows) I shilighted in short-T2 image.

In Figure 5.7, we compared performance of the previously described Inverted Double Half RF pulse (IDHRF) (97) used to null excitation of fat and longer T2 species with the IDEAL-UTE in the Achilles tendon. While IDHRF showed the desired suppression near the Achilles tendon, it

fails in other areas (red arrows) due to errors in field inhomogeneity. The short T2 image of the IDEAL-UTE shows enhanced depiction of the Achilles tendon, other tendons not visualized in the IDHRF image, and uniform fat and water suppression over the entire joint. The fractions of short and long T2 components can also be obtained from water and short T2 images.

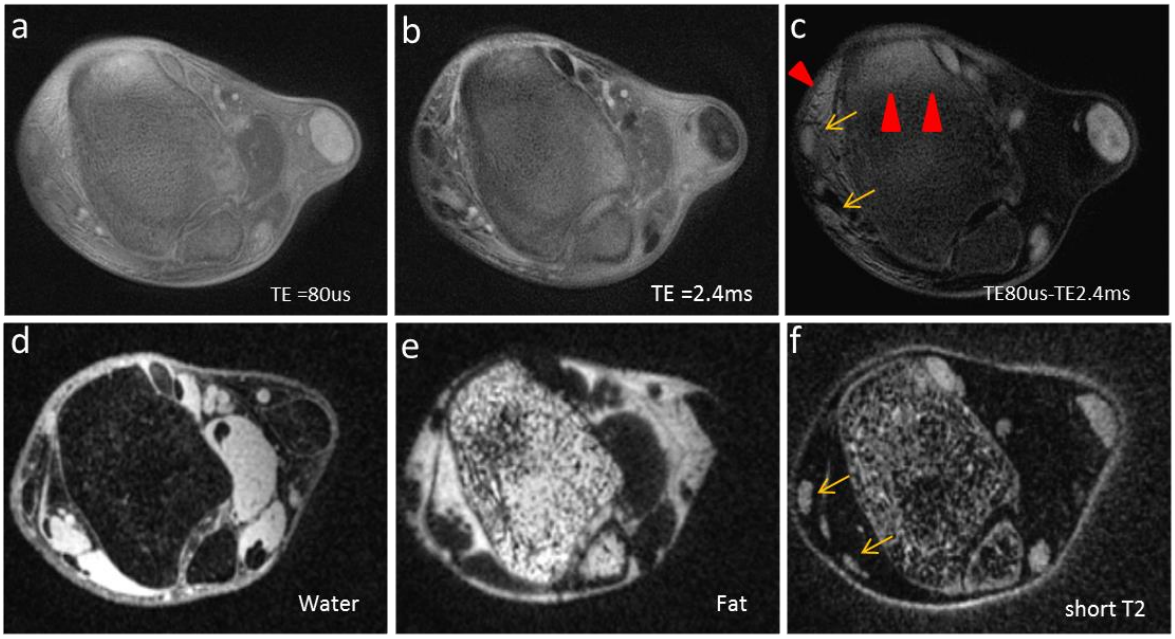

Figure 5.7 Axial images of IDHRF UTE, short TE (a), second echo (b), subtraction (c) and IDEAL UTE water image (d), IDEAL fat image (e) and IDEAL short-T2 image (f). IDHRF UTE failed to completely suppress long-T2 components (red arrows) due to B0 inhomogeneity.

5.4 Conclusion

The modified Inverted double half pulse with time delay between the two half pulses selected for fat saturation, improves fat suppression and increase the dynamic range for short T2 components at no additional cost in imaging time. This IDHRF pulse selectively inverts long-*T*2 species, which can be suppressed by also acquiring an image where they are not inverted and then combining these images.

The 3D UTE SPGR sequence with multi-echo acquisition and IDEAL reconstruction provides high contrast imaging of short T2 species despite B0 inhomogeneity while also robustly suppressing fat. It also provides high contrast short T2-only images as well as a uniform fat and water separation images and R*2 map all in a single acquisition.

Chapter 6:

Summary and Future Work

6.1 Summary

The contributions of this dissertation can be summarized as follows:

Radial Fat Suppressed Alternating Repetition Time bSSFP Imaging

Fat suppressed Alternating TR bSSFP imaging method has been combined with the 3D radial dual-half echo trajectory to provide fat-suppressed knee images with high isotropic resolution for whole joint assessment at 3T. The method was qualitatively and quantitatively compared with other currently used fat-suppressed 3D sequences for evaluating the articular cartilage of the knee joint at 3.0T on both knee joints of five asymptomatic volunteers. Dramatic improvements in image quality and signal-to-noise ratio were achieved with Radial FS-ATR. The implications of this work include improved visualization of the articular cartilage of the knee joint, and acquisition of multiplanar fat-suppressed images of the knee joint with high isotropic resolution at 3T. This work has been published in the journal of Magnetic Resonance imaging.

3D IDEAL Ultrashort TE (UTE) Imaging

IDEAL reconstruction algorithm was modified to account for signal from short-T2 components. This reconstruction technique has been combined with the 3D radial multi-echo Ultra Short TE

imaging to separates short T2 water signal, longer T2 water signal, and lipid signal. The method was applied in phantom and volunteer studies and provided improved fat and water suppression and improved short T2 components visualization in tendon and meniscus joints. Implications of this method include improved depiction of short-T2 components with high image contrast. IDEAL chemical shift decomposition with robust B0 correction allows visualization of tissues with short-T2 relaxation in areas that have susceptibility changes such as chest. A manuscript for publication is in preparation.

Quantification of 3D Radial Undersampling Artifacts

A method has been developed to quantitatively and qualitatively measure the effects of 3D undersampling in vivo using 8 channel knee coil and investigate the advantage of increased number of coil elements in the azimuthal dimension. The method was applied in phantom and volunteer studies. Results demonstrate a non-uniform distribution of aliased energy due to undersampling in radial trajectory and showed significant reduction in undersampling artifacts using 16 channel coil. Implications of this research include the ability to accelerate data acquisition to either maintain the same resolution with a reduction in scan time, or achieve higher resolution while maintaining the same scan time; potentially boost image SNR and CNR; and move towards real-time interventional procedures.

Imaging of Joint Structure with Limited Free Water Using UTE

An Inverted double half RF excitation pulse has been developed for 2D radial imaging to selectively excite short-T2 tissue and suppress long-T2 water and lipids signal to improve short-T2 species image contrast and reduce eddy current errors. The method was implemented in phantom and in vivo studies and demonstrated improved dynamic range for short T2 components in tendon and knee meniscus. The RF pulse presented in this work demonstrated an improved excitation profile for imaging short T2 tissues and provided an effective alternative to the time-consuming gradient characterization and compensation techniques, and can be especially useful for quantitation of short T2 spins.

6.2 Future Work

Radial Fat Suppressed Alternating Repetition Time bSSFP Imaging

In contrast to conventional bSSFP, FS-ATR bSSFP uses more RF pulses for the same amount of readout time. RF heating is an important constraint for this sequence and so the flip angle has been reduced to maintain SAR. However, reduced flip angle lead to suboptimal SNR and CNR. In other hand, the null-to-null spacing in FS-ATR is dependent on the flip angle and get close to 2/TR with lower angles. Investigation should be performed to determine the optimal flip angle that maximize the SNR efficiency for cartilage and minimize undesired signal nulling in the image. Fat suppression in the Radial FS-ATR sequence is also assessed by the progression during the two half echoes within each TR. Future investigation of Radial FS-ATR sequence should also include the optimization of the echo spacing during data acquisition in TR1 for the desired isotropic resolution to improve the inherent fat suppression.

Future studies are needed to determine whether Radial-ATR can be used to detect early cartilage degeneration in clinical practice and to provide rapid "whole-organ" joint assessment and cartilage volume analysis in osteoarthritis research studies. Furthermore, evaluation of other joint structures such as menisci, ligaments and bone marrow with FS-ATR should also be investigated.

The need to assess the cartilage surface of the hip joint, with its thin surfaces over the sloping ball of the femur, is a more pressing need in diagnostic radiology today. Such imaging is crucial for the proper assessment of the causes of hip pain, a problem facing people at earlier and earlier ages today. The relatively thin cartilage of the hip joint, as well as its complex geometry, poses challenges for standardized, reproducible assessment of cartilage and the acetabular labrum. High resolution morphologic cartilage imaging techniques are needed to improve sensitivity to early changes in cartilage volume, allowing for faster evaluation of new OA hypotheses and treatment options.

As an initial study examining the feasibility of VIPR-ATR to produce high resolution hip images, a volunteer was imaged with the 3D radial FS-ATR sequence on a 3.0T Discovery MR750 scanner (GE Healthcare, Milwaukee, WI) using a 32 channel phased-array torso coil. Each scan was acquired in 8 minutes with the following parameters: 15° flip angle, 20cm FOV covering only one hip joint, 400 x 400 x 400 image matrix, and ±125 kHz receiver BW.

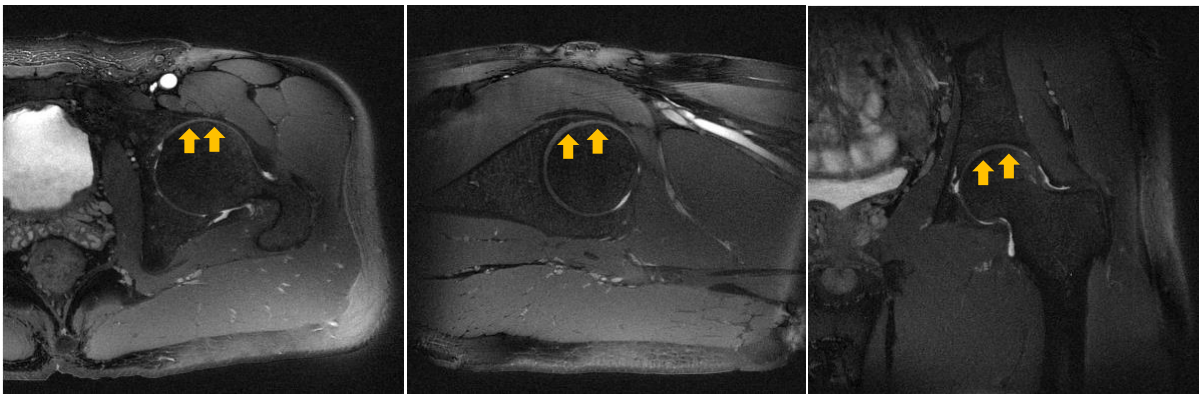

Figure 6.1 0.5 mm isotropic resolution reformats in the axial, sagittal, and coronal planes show details of the cartilage, bone, and fluid interfaces of the 3D radial FS-ATR acquired hip joint. Note the fine depiction of the cartilage surfaces (arrowheads).

The ability of 3D FS-ATR to provide 0.5 mm isotropic resolution, as shown in Figure 6.1, demonstrates that this method would be useful in cartilage assessment. The hip images in Figure 6.1, reformatted to show axial, sagittal, and coronal views, give excellent high resolution depiction of cartilage with consistent fat suppression over the joint and high cartilage/fluid and cartilage/bone CNR. Additional hip patients must be acquired using this method to extend the use of VIPR-ATR to image hip cartilage and determine its capability to evaluate hip joint structures. Other joint and vasculature applications should be explored for each of our FS-ATR sequences. Possible sites of interest include the wrist, hip, ankle, shoulder and cervical spine.

3D IDEAL Ultrashort TE (UTE) Imaging

Fat and water separation in IDEAL decomposition depends on the echo spacing. The optimal TE spacing that maximizes the number of signal averages occurs when the phase differences between fat and water are evenly distributed around the unit circle(41). However, for IDEAL-

UTE reconstruction, we pre-assumed that the T_2 of the short-T_2 spices is very short that it decays before second echo occurs. Future investigation of IDEAL-UTE sequence should include the optimization of the echo spacing during data acquisition to maximize SNR efficiency while maintaining the short-T_2 assumption.

In the near future, further study is needed to assess pathologic changes in the deep cartilage layer secondary to osteochondral injuries in patients with ACL tear. Osteochondral injuries are extremely common in patients with ACL tears and may responsible for the high incidence of osteoarthritis noted in this patient population despite successful ligament reconstruction surgery. Quantitative MRI techniques have shown changes in the superficial cartilage overlying areas of osteochondral injuries in patients with ACL tears. However, the deep cartilage layer is unable to be assessed since its short T2 components cannot be detected using conventional MRI techniques. A study to investigate the ability of IDEAL-UTE imaging to detect pathologic changes in the deep cartilage layer in patients with ACL tears would be needed.

References

1. Anon. From the Centers for Disease Control and Prevention. revalence and activity limitations--United StateArthritis ps, 1990. Jama 1994;272:346–7.

2. Anon. From the Centers for Disease Control and Prevention. Targeting arthritis: reducing disability for 43 million Americans. At-A-Glance 2005.

3. Felson DT. An update on the pathogenesis and epidemiology of osteoarthritis. Radiol. Clin. North Am. [Internet] 2004;42:1–9, v. doi: 10.1016/S0033-8389(03)00161-1.

4. Felson DT, Zhang Y. An update on the epidemiology of knee and hip osteoarthritis with a view to prevention. Arthritis Rheum. [Internet] 1998;41:1343–55. doi: 10.1002/1529-0131(199808)41:8<1343::AID-ART3>3.0.CO;2-9.

5. Oliveria SA, Felson DT, Reed JI, Cirillo PA, Walker AM. Incidence of symptomatic hand, hip, and knee osteoarthritis among patients in a health maintenance organization. Arthritis Rheum. [Internet] 1995;38:1134–41.

6. Lawrence RC, Helmick CG, Arnett FC, et al. Estimates of the prevalence of arthritis and selected musculoskeletal disorders in the United States. Arthritis Rheum. [Internet] 1998;41:778–99. doi: 10.1002/1529-0131(199805)41:5<778::AID-ART4>3.0.CO;2-V.

7. PETERFY C, WOODWORTH T, ALTMAN R. Workshop for Consensus on Osteoarthritis Imaging: MRI of the knee. Osteoarthr. Cartil. [Internet] 2006;14:44–45. doi: 10.1016/j.joca.2006.02.025.

8. Hill CL, Gale DG, Chaisson CE, Skinner K, Kazis L, Gale ME, Felson DT. Knee effusions, popliteal cysts, and synovial thickening: association with knee pain in osteoarthritis. J. Rheumatol. [Internet] 2001;28:1330–7.

9. Sowers MF, Hayes C, Jamadar D, Capul D, Lachance L, Jannausch M, Welch G. Magnetic resonance-detected subchondral bone marrow and cartilage defect characteristics associated with pain and X-ray-defined knee osteoarthritis. Osteoarthritis Cartilage [Internet] 2003;11:387–93.

10. Peterfy CG, Gold G, Eckstein F, Cicuttini F, Dardzinski B, Stevens R. MRI protocols for whole-organ assessment of the knee in osteoarthritis. Osteoarthritis Cartilage [Internet] 2006;14 Suppl A:A95–111. doi: 10.1016/j.joca.2006.02.029.

11. Hochberg MC, Lawrence RC, Everett DF, Cornoni-Huntley J. Epidemiologic associations of pain in osteoarthritis of the knee: data from the National Health and Nutrition Examination Survey and the National Health and Nutrition Examination-I Epidemiologic Follow-up Survey. Semin. Arthritis Rheum. [Internet] 1989;18:4–9.

12. Hirasawa Y, Okajima S, Ohta M, Tokioka T. Nerve distribution to the human knee joint: anatomical and immunohistochemical study. Int. Orthop. [Internet] 2000;24:1–4.

13. Felson DT, Chaisson CE, Hill CL, Totterman SM, Gale ME, Skinner KM, Kazis L, Gale DR. The association of bone marrow lesions with pain in knee osteoarthritis. Ann. Intern. Med. [Internet] 2001;134:541–9.

14. Conaghan PG, Felson D, Gold G, Lohmander S, Totterman S, Altman R. MRI and non-cartilaginous structures in knee osteoarthritis. Osteoarthritis Cartilage [Internet] 2006;14 Suppl A:A87–94. doi: 10.1016/j.joca.2006.02.028.

15. Peterfy CG, Guermazi A, Zaim S, et al. Whole-Organ Magnetic Resonance Imaging Score (WORMS) of the knee in osteoarthritis. Osteoarthritis Cartilage [Internet] 2004;12:177–90. doi: 10.1016/j.joca.2003.11.003.

16. Hardingham T, Bayliss M. Proteoglycans of articular cartilage: changes in aging and in joint disease. Semin. Arthritis Rheum. [Internet] 1990;20:12–33.

17. Mlynárik V, Trattnig S. Physicochemical properties of normal articular cartilage and its MR appearance. Invest. Radiol. [Internet] 2000;35:589–94.

18. Pullig O, Kladny B, Weseloh G, Swoboda B. [Metabolic activation of chondrocytes in human osteoarthritis. Expression of type II collagen]. Z. Orthop. Ihre Grenzgeb. [Internet] 137:67–75. doi: 10.1055/s-2008-1037039.

19. Dunn TC, Lu Y, Jin H, Ries MD, Majumdar S. T2 relaxation time of cartilage at MR imaging: comparison with severity of knee osteoarthritis. Radiology [Internet] 2004;232:592–8. doi: 10.1148/radiol.2322030976.

20. Goodwin DW, Dunn JF. High-resolution magnetic resonance imaging of articular cartilage: correlation with histology and pathology. Top. Magn. Reson. Imaging [Internet] 1998;9:337–47.

21. Goodwin DW, Wadghiri YZ, Zhu H, Vinton CJ, Smith ED, Dunn JF. Macroscopic structure of articular cartilage of the tibial plateau: influence of a characteristic matrix architecture on MRI appearance. AJR. Am. J. Roentgenol. [Internet] 2004;182:311–8. doi: 10.2214/ajr.182.2.1820311.

22. Liess C, Lüsse S, Karger N, Heller M, Glüer C-C. Detection of changes in cartilage water content using MRI T2-mapping in vivo. Osteoarthritis Cartilage [Internet] 2002;10:907–13.

23. Mosher TJ, Collins CM, Smith HE, Moser LE, Sivarajah RT, Dardzinski BJ, Smith MB. Effect of gender on in vivo cartilage magnetic resonance imaging T2 mapping. J. Magn. Reson. Imaging [Internet] 2004;19:323–8. doi: 10.1002/jmri.20013.

24. Wheaton AJ, Borthakur A, Shapiro EM, Regatte RR, Akella SVS, Kneeland JB, Reddy R. Proteoglycan loss in human knee cartilage: quantitation with sodium MR imaging--feasibility study. Radiology [Internet] 2004;231:900–5. doi: 10.1148/radiol.2313030521.

25. Duvvuri U, Reddy R, Patel SD, Kaufman JH, Kneeland JB, Leigh JS. T1rho-relaxation in articular cartilage: effects of enzymatic degradation. Magn. Reson. Med. [Internet] 1997;38:863–7.

26. Bashir A, Gray ML, Boutin RD, Burstein D. Glycosaminoglycan in articular cartilage: in vivo assessment with delayed Gd(DTPA)(2-)-enhanced MR imaging. Radiology [Internet] 1997;205:551–8. doi: 10.1148/radiology.205.2.9356644.

27. Kim Y-J, Jaramillo D, Millis MB, Gray ML, Burstein D. Assessment of early osteoarthritis in hip dysplasia with delayed gadolinium-enhanced magnetic resonance imaging of cartilage. J. Bone Joint Surg. Am. [Internet] 2003;85-A:1987–92.

28. Barger A V, Block WF, Toropov Y, Grist TM, Mistretta CA. Time-resolved contrast-enhanced imaging with isotropic resolution and broad coverage using an undersampled 3D projection trajectory. Magn. Reson. Med. [Internet] 2002;48:297–305. doi: 10.1002/mrm.10212.

29. Block F, Barger A V, Mistretta CA. Vastly Undersampled Isotropic Projection Imaging. 2000;8:2000.

30. Lu A, Brodsky E, Grist TM, Block WF. Rapid fat-suppressed isotropic steady-state free precession imaging using true 3D multiple-half-echo projection reconstruction. Magn. Reson. Med. 2005;53:692–699.

31. Scheffler K, Lehnhardt S. Principles and applications of balanced SSFP techniques. Eur. Radiol. 2003;13:2409–2418.

32. Leupold J, Hennig J, Scheffler K. Alternating repetition time balanced steady state free precession. Magn. Reson. Med. 2006;55:557–565.

33. Cukur T, Nishimura DG. Multiple repetition time balanced steady-state free precession imaging. Magn. Reson. Med. 2009;62:193–204.

34. J.L. Klaers, E. K. Brodesky, W.F. Block et al. High Resolution Cartilage and Whole Organ Knee Joint Assessment: 3D Radial Fat-Suppressed Alternating TR SSFP. In: ISMRM. ; 2010.

35. Klaers J, Jashnani Y, Jung Y, Brodsky E, Jacobson J, Kijowski R, Block WF. Dual half-echo phase correction for implementation of 3D radial SSFP at 3.0 T. Magn. Reson. Med. 2010;63:282–289.

36. Tyler DJ, Robson MD, Henkelman RM, Young IR, Bydder GM. Magnetic resonance imaging with ultrashort TE (UTE) PULSE sequences: technical considerations. J. Magn. Reson. Imaging 2007;25:279–289.

37. Robson MD, Gatehouse PD, Bydder M, Bydder GM. Magnetic resonance: an introduction to ultrashort TE (UTE) imaging. J. Comput. Assist. Tomogr. [Internet] 27:825–46.

38. Glover GH, Pauly JM, Bradshaw KM. Boron-11 imaging with a three-dimensional reconstruction method. J. Magn. Reson. Imaging [Internet] 2:47–52.

39. Wu Y, Ackerman JL, Chesler DA, Graham L, Wang Y, Glimcher MJ. Density of organic matrix of native mineralized bone measured by water- and fat-suppressed proton projection MRI. Magn. Reson. Med. [Internet] 2003;50:59–68. doi: 10.1002/mrm.10512.

40. Rahmer J, Börnert P, Groen J, Bos C. Three-dimensional radial ultrashort echo-time imaging with T2 adapted sampling. Magn. Reson. Med. [Internet] 2006;55:1075–82. doi: 10.1002/mrm.20868.

41. Reeder SB, Wen Z, Yu H, Pineda AR, Gold GE, Markl M, Pelc NJ. Multicoil Dixon chemical species separation with an iterative least-squares estimation method. Magn. Reson. Med. 2004;51:35–45.

42. Haase A, Frahm J, Hänicke W, Matthaei D. 1H NMR chemical shift selective (CHESS) imaging. Phys. Med. Biol. [Internet] 1985;30:341–4.

43. Meyer CH, Pauly JM, Macovski A, Nishimura DG. Simultaneous spatial and spectral selective excitation. Magn. Reson. Med. [Internet] 1990;15:287–304.

44. Bydder GM, Young IR. MR imaging: clinical use of the inversion recovery sequence. J Comput Assist Tomogr 1985;9:659–675.

45. Dixon WT. Simple proton spectroscopic imaging. Radiology 1984;153:189–194.

46. Yeung HN, Kormos DW. Separation of true fat and water images by correcting magnetic field inhomogeneity in situ. Radiology 1986;159:783–786.

47. Glover GH, Schneider E. Three-point Dixon technique for true water/fat decomposition with B0 inhomogeneity correction. Magn. Reson. Med. [Internet] 1991;18:371–83.

48. Glover GH. Multipoint Dixon technique for water and fat proton and susceptibility imaging. J. Magn. Reson. Imaging [Internet] 1:521–30.

49. Reeder SB, Pineda AR, Wen Z, Shimakawa A, Yu H, Brittain JH, Gold GE, Beaulieu CH, Pelc NJ. Iterative decomposition of water and fat with echo asymmetry and least-squares estimation (IDEAL): application with fast spin-echo imaging. Magn. Reson. Med. [Internet] 2005;54:636–44. doi: 10.1002/mrm.20624.

50. Gold GE, Reeder SB, Yu H, Kornaat P, Shimakawa AS, Johnson JW, Pelc NJ, Beaulieu CF, Brittain JH. Articular cartilage of the knee: rapid three-dimensional MR imaging at 3.0 T with IDEAL balanced steady-state free precession--initial experience. Radiology 2006;240:546–551.

51. Siepmann D, Reeder S, McGovern J, Brittain J, Gold G. High resolution 3D cartilage imaging of the knee at 3T in five minutes using IDEAL-SPGR and parallel imaging. In: Proceedings 14th Scientific Meeting International Society for Magnetic Resonance in Medicine. ; 2006. p. 1251.

52. Rubenstein JD, Li JG, Majumdar S, Henkelman RM. Image resolution and signal-to-noise ratio requirements for MR imaging of degenerative cartilage. Ajr Am. J. Roentgenol. 1997;169:1089–1096.

53. Hardya PA, Newmark R, Liu YM, Meier D, Norris S, Piraino DW, Shah A. The influence of the resolution and contrast on measuring the articular cartilage volume in magnetic resonance images. Magn. Reson. Imaging 2000;18:965–972.

54. Kijowski R, Lu A, Block W, Grist T. Evaluation of the articular cartilage of the knee joint with vastly undersampled isotropic projection reconstruction steady-state free precession imaging. J. Magn. Reson. Imaging 2006;24:168–175.

55. Gold GE, Hargreaves BA, Vasanawala SS, Webb JD, Shimakawa AS, Brittain JH, Beaulieu CF. Articular cartilage of the knee: evaluation with fluctuating equilibrium MR imaging--initial experience in healthy volunteers. Radiology 2006;238:943–949.

56. Hargreaves BA, Gold GE, Beaulieu CF, Vasanawala SS, Nishimura DG, Pauly JM. Comparison of new sequences for high-resolution cartilage imaging. Magn. Reson. Med. 2003;49:700–709.

57. Disler DG, McCauley TR, Kelman CG, Fuchs MD, Ratner LM, Wirth CR, Hospodar PP. Fat-suppressed three-dimensional spoiled gradient-echo MR imaging of hyaline cartilage defects in the knee: comparison with standard MR imaging and arthroscopy. Ajr Am. J. Roentgenol. 1996;167:127–132.

58. Kijowski R, Tuite M, Passov L, Shimakawa A, Yu H, Reeder SB. Cartilage imaging at 3.0T with gradient refocused acquisition in the steady-state (GRASS) and IDEAL fat-water separation. J. Magn. Reson. Imaging 2008;28:167–174.

59. Hardy PA, Recht MP, Piraino D, Thomasson D. Optimization of a dual echo in the steady state (DESS) free-precession sequence for imaging cartilage. J. Magn. Reson. Imaging 1996;6:329–335.

60. Gold GE, Fuller SE, Hargreaves BA, Stevens KJ, Beaulieu CF. Driven equilibrium magnetic resonance imaging of articular cartilage: initial clinical experience. J. Magn. Reson. Imaging 2005;21:476–481.

61. Kijowski R, Davis KW, Woods MA, Lindstrom MJ, De Smet AA, Gold GE, Busse RF. Knee joint: comprehensive assessment with 3D isotropic resolution fast spin-echo MR imaging--diagnostic performance compared with that of conventional MR imaging at 3.0 T. Radiology 2009;252:486–495.

62. Kijowski R, Blankenbaker DG, Klaers JL, Shinki K, De Smet AA, Block WF. Vastly undersampled isotropic projection steady-state free precession imaging of the knee: diagnostic performance compared with conventional MR. Radiology 2009;251:185–194.

63. Sequence WTF, Koch P, Schmid MR, Pfirrmann CWA. Diagnosis of Articular Cartilage Abnormalities of the Knee : Prospective Clinical Evaluation of a 3D Methods : Results : Conclusion. Evaluation 2007;243:475–482.

64. Scheffler K, Heid O, Hennig J. Magnetization preparation during the steady state: fat-saturated 3D TrueFISP. Magn. Reson. Med. 2001;45:1075–1080.

65. Kornaat PR, Doornbos J, Van Der Molen AJ, Kloppenburg M, Nelissen RG, Hogendoorn PCW, Bloem JL. Magnetic resonance imaging of knee cartilage using a water selective balanced steady-state free precession sequence. J. Magn. Reson. Imaging 2004;20:1235–1240. doi: 10.1002/jmri.22529.

66. Vasanawala SS, Pauly JM, Nishimura DG. Fluctuating equilibrium MRI. Magn. Reson. Med. 1999;42:876–883.

67. Vasanawala SS, Pauly JM, Nishimura DG. Linear combination steady-state free precession MRI. Magn. Reson. Med. 2000;43:82–90.

68. Nayak KS, Lee H-L, Hargreaves BA, Hu BS. Wideband SSFP: alternating repetition time balanced steady state free precession with increased band spacing. Magn. Reson. Med. 2007;58:931–938.

69. Chen CA, Kijowski R, Shapiro LM, Tuite MJ, Davis KW, Klaers JL, Block WF, Scott B, Gold GE. Cartilage Morphology at 3 . 0T : Assessment of Three-Dimensional MR Imaging Techniques. J. Magn. Reson. 2010;32:173–183. doi: 10.1002/jmri.22213.Cartilage.

70. Reeder SB, McKenzie CA, Pineda AR, Yu H, Shimakawa A, Brau AC, Hargreaves BA, Gold GE, Brittain JH. Water-fat separation with IDEAL gradient-echo imaging. J. Magn. Reson. Imaging [Internet] 2007;25:644–52. doi: 10.1002/jmri.20831.

71. Dietrich O, Raya JG, Reeder SB, Reiser MF, Schoenberg SO. Measurement of signal-to-noise ratios in MR images: influence of multichannel coils, parallel imaging, and reconstruction filters. J. Magn. Reson. Imaging 2007;26:375–385.

72. Welsch GH, Juras V, Szomolanyi P, Mamisch TC, Baer P, Kronnerwetter C, Blanke M, Fujita H, Trattnig S. Magnetic resonance imaging of the knee at 3 and 7 Tesla: a comparison using dedicated multi-channel coils and optimised 2D and 3D protocols. Eur. Radiol. 2012;22:1852–9. doi: 10.1007/s00330-012-2450-1.

73. Friedrich KM, Reiter G, Kaiser B, Mayerhöfer M, Deimling M, Jellus V, Horger W, Trattnig S, Schweitzer M, Salomonowitz E. High-resolution cartilage imaging of the knee at 3T: basic evaluation of modern isotropic 3D MR-sequences. Eur. J. Radiol. 2011;78:398–405.

74. Cukur T, Nishimura DG. Fat-water separation with alternating repetition time balanced SSFP. Magn. Reson. Med. 2008;60:479–484.

75. Lee KJ, Lee H-L, Hennig J, Leupold J. Use of simulated annealing for the design of multiple repetition time balanced steady-state free precession imaging. Magn. Reson. Med. [Internet] 2012;68:220–6. doi: 10.1002/mrm.23221.

76. Duc SR, Pfirrmann CWA, Koch PP, Zanetti M, Hodler J. Internal knee derangement assessed with 3-minute three-dimensional isovoxel true FISP MR sequence: preliminary study. Radiology 2008;246:526–535.

77. Bae WC, Chen PC, Chung CB, Masuda K, D'Lima D, Du J. Quantitative ultrashort echo time (UTE) MRI of human cortical bone: correlation with porosity and biomechanical properties. J. Bone Miner. Res. [Internet] 2012;27:848–57. doi: 10.1002/jbmr.1535.

78. Biswas R, Bae W, Diaz E, Masuda K, Chung CB, Bydder GM, Du J. Ultrashort echo time (UTE) imaging with bi-component analysis: bound and free water evaluation of bovine cortical bone subject to sequential drying. Bone [Internet] 2012;50:749–55. doi: 10.1016/j.bone.2011.11.029.

79. Pauli C, Bae WC, Lee M, Lotz M, Bydder GM, D'Lima DL, Chung CB, Du J. Ultrashort-echo time MR imaging of the patella with bicomponent analysis: correlation with histopathologic and polarized light microscopic findings. Radiology [Internet] 2012;264:484–93. doi: 10.1148/radiol.12111883.

80. Du J, Carl M, Bydder M, Takahashi A, Chung CB, Bydder GM. Qualitative and quantitative ultrashort echo time (UTE) imaging of cortical bone. J. Magn. Reson. [Internet] 2010;207:304–11. doi: 10.1016/j.jmr.2010.09.013.

81. Du J, Diaz E, Carl M, Bae W, Chung CB, Bydder GM. Ultrashort echo time imaging with bicomponent analysis. Magn. Reson. Med. [Internet] 2012;67:645–9. doi: 10.1002/mrm.23047.

82. Du J, Bydder GM. Qualitative and quantitative ultrashort-TE MRI of cortical bone. NMR Biomed. [Internet] 2013;26:489–506. doi: 10.1002/nbm.2906.

83. Gatehouse PD, Bydder GM. Magnetic resonance imaging of short T2 components in tissue. Clin. Radiol. 2003;58:1–19.

84. Rodriguez W, Vinson EN, Helms CA, Toth AP. MRI appearance of posterior cruciate ligament tears. AJR. Am. J. Roentgenol. [Internet] 2008;191:1031. doi: 10.2214/AJR.07.2921.

85. Schweitzer ME, Karasick D. MR imaging of disorders of the Achilles tendon. AJR. Am. J. Roentgenol. [Internet] 2000;175:613–25. doi: 10.2214/ajr.175.3.1750613.

86. Larson PEZ, Conolly SM, Pauly JM, Nishimura DG. Using adiabatic inversion pulses for long-T2 suppression in ultrashort echo time (UTE) imaging. Magn. Reson. Med. [Internet] 2007;58:952–61. doi: 10.1002/mrm.21341.

87. Du J, Takahashi AM, Bae WC, Chung CB, Bydder GM. Dual inversion recovery, ultrashort echo time (DIR UTE) imaging: creating high contrast for short-T(2) species. Magn. Reson. Med. [Internet] 2010;63:447–55. doi: 10.1002/mrm.22257.

88. Qian Y, Williams AA, Chu CR, Boada FE. Multicomponent T2* mapping of knee cartilage: technical feasibility ex vivo. Magn. Reson. Med. [Internet] 2010;64:1426–31. doi: 10.1002/mrm.22450.

89. Du J, Takahashi AM, Bydder M, Chung CB, Bydder GM. Ultrashort TE imaging with off-resonance saturation contrast (UTE-OSC). Magn. Reson. Med. [Internet] 2009;62:527–31. doi: 10.1002/mrm.22007.

90. Du J, Bydder M, Takahashi AM, Carl M, Chung CB, Bydder GM. Short T2 contrast with three-dimensional ultrashort echo time imaging. Magn. Reson. Imaging [Internet] 2011;29:470–482.

91. Wang K, Yu H, Brittain JH, Reeder SB, Du J. k-space water-fat decomposition with T2* estimation and multifrequency fat spectrum modeling for ultrashort echo time imaging. J. Magn. Reson. Imaging [Internet] 2010;31:1027–34. doi: 10.1002/jmri.22121.

92. Yu H, Shimakawa A, McKenzie CA, Brodsky E, Brittain JH, Reeder SB. Multiecho water-fat separation and simultaneous R2* estimation with multifrequency fat spectrum modeling. Magn. Reson. Med. [Internet] 2008;60:1122–34. doi: 10.1002/mrm.21737.

93. Klaers, JK, Brodsky E and, Block W. Quantification of 3D Radial Undersampling Artifact to Obtain High Quality Isotropic Resolution (0.36 mm) for Volumetric Cartilage Assessment.

94. Griswold MA, Jakob PM, Heidemann RM, Nittka M, Jellus V, Wang J, Kiefer B, Haase A. Generalized autocalibrating partially parallel acquisitions (GRAPPA). Magn. Reson. Med. 2002;47:1202–1210.

95. Pauly JM, Conolly SM, Nishimura DG MA. Slice-selective excitation for very short T2 species. In: SMRM. ; 1989. p. 28.

96. Josan S, Pauly JM, Daniel BL, Pauly KB. Double half RF pulses for reduced sensitivity to eddy currents in UTE imaging. Magn. Reson. Med. 2009;61:1083–1089.

97. H. Al saleh, K.M. Johnson, W.F. Block RK. Inverted Double Half RF Pulses: Improved Selective Excitation of Short T2 Components in 3T Joint Imaging. In: ISMRM. ; 2011.